Water in Plagioclase Phenocrysts from the 2009 Eruption of Redoubt Volcano, Alaska

Robert Stutzke

04/23/2024

Advisors: Dr. Megan Newcombe and Sumedha Desikamani

GEOL 394

Thesis submitted to the Faculty of the Department of Geology
of the University of Maryland, College Park, in partial fulfillment
of the requirements for the degree of
Bachelor of Science
2024

Contents

Table of Figures

Table of Tables

Table of Equations

Abstract

Current petrologic methods constraining the hour to month timescales of pre-eruptive magma migration lack the resolution of depth that could be used to interpret seismic precursor signals through time and space. Water in plagioclase feldspar has potential as a hygrometer on seismic precursor timescales and may potentially track magma migration in the hours to weeks prior to eruption. This study measured water in plagioclase feldspar using Fourier Transform Infrared (FTIR) spectroscopy to estimate pre-eruptive magma storage depths for eruption Events 5 and 6 from the 2009 eruption of Redoubt Volcano. Calculated plagioclase H_2O concentrations varied from 12 ± 4 – 1165 ± 350 ppm (1σ). Calculated depths range from 0.12 ± 0.04 to > 34 km. Calculated depth ranges generally did not agree with petrologic estimations of storage depths given by Coombs et al. (2013) and Hosseini et al. (2023) (4 – 6 km and 4.9 – 12.3 km, respectively), though there may be some agreement with the low-silica andesite (LSA) deep source region situated between 30 – 40 km as suggested by Coombs et al. (2013). Additionally, depth ranges do not agree with geodetic estimations of mid-crustal storage of 10 – 14.5 km (Grapenthin et al., 2013). There is some agreement between calculated depths and geophysical observations of seismic activity, with the shallow calculated depths falling within the range of hypocenter depths observed during the P1 seismic swarm (0 – 7 km; Bull and Buurman, 2013; Buurman et al., 2013). All studied crystals fall outside the range of mid-crustal seismicity (3 – 9 km; Power et al., 2013) but there may be some agreement with the deep long period-earthquakes (DLPs) that occurred between 28 – 41 km in December of 2008 (Power et al., 2013) associated with a deep, diffuse magma source region. Study methodology complicated interpretation of recorded water concentrations, suggesting recorded water concentrations are unlikely to be completely representative of purely structurally bound OH^-, systematically overestimating calculated storage depths. Future studies must address these methodological complications if the plagioclase hygrometer is to become a reliable indicator of host-melt water contents.

Plain-text Abstract

Volcanic eruptions threaten human health and productivity. Accurate eruption forecasting remains a challenge, even in well-monitored volcanic systems. Pre-eruptive geophysical observations understood within a post-eruptive petrologic context may help inform future forecasting efforts by tying pattern recognition to a more mechanistic understanding of magma storage and migration in volcanic systems. In this study, water in plagioclase was used to determine the storage depth recorded by materials ejected during Events 5 and 6 of the 2009 eruption of Redoubt Volcano, Alaska. Depths were then compared to the P1 seismic swarm immediately preceding the first magmatic explosion on March 23rd to see if there is any observable relationship. It was found that most measured plagioclase grains indicated a storage depth of > 34 km, with one measured grain indicating a storage depth of around 200 m. Calculated depths are overestimated due to complications in study methodology. Future work should address these complications to better constrain water concentrations recorded by plagioclase feldspar.

1. Introduction and Background

1.1 The Geography and Geology of Redoubt Volcano

Redoubt Volcano (hereafter referred to as "Redoubt") is an andesitic stratovolcano located west of the Cook Inlet, approximately 170 km southwest of Anchorage, Alaska (Figure 1). Redoubt is part of the Chigmit Mountains, the northeast segment of the Aleutian volcanic arc comprising more than 100 primarily andesitic volcanoes (Bull and Buurman, 2013). The base of Redoubt is approximately 1350 m above sea level (ASL); its summit is approximately 3110 m ASL. All depths mentioned hereafter are in reference to the 3 km summit (i.e., at the summit, depth is equal to zero). It has a basal diameter of 10 – 12 km and an approximate edifice volume of 40 km^3 (Till et al., 1994). Its edifice is 100 – 110 km above the Benioff zone and 450 km northwest of the Aleutian trench (Kienle and Swanson, 1983). Most of the volcano is ice-covered; the northern rim of its 1.5 km wide crater is incised by the Drift Glacier. This glacier flows north and terminates on the Drift River Valley floor, near the headwaters of the Drift River. The Drift River flows 35 km east from the glacier to the Cook Inlet. Many human populations surround Cook Inlet, including Alaska's largest population center, Anchorage.

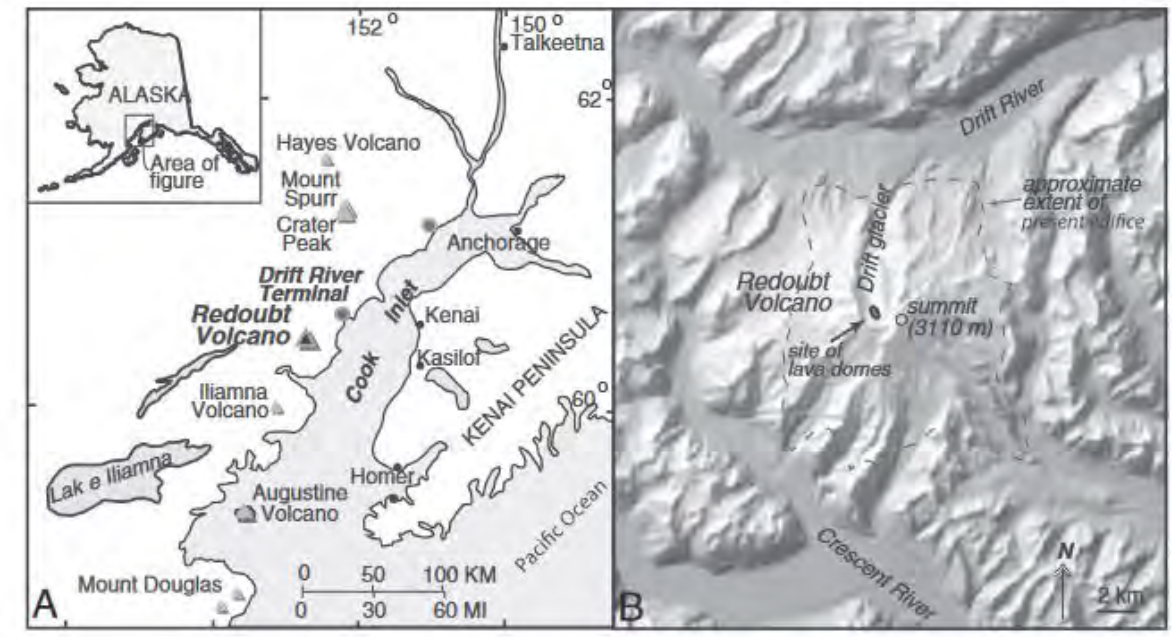

Figure 1: Location of Redoubt Volcano from (Bull and Buurman, 2013). (A) Regional scale map of the Cook Inlet. Note the positions of Redoubt and other volcanoes, the Drift River Terminal (DRT), a crude oil storage facility, and Anchorage. (B) Shaded-relief map of Redoubt, with locations of lava domes emplaced during the 1966-68, 1989-90, and 2009 eruptions.

Redoubt's edifice is composed of mid-Pleistocene to Holocene dacitic to basaltic pyroclastic-density-current (PDC) deposits, block-and-ash-flow deposits, and lava flows, on top of Jurassic quartz diorites and tonalites of the Alaska-Aleutian Range batholith (Till

et al., 1994; Reed and Lanphere, 1974), all underlain by a Proterozoic basement (Bacon et al., 2012; Detterman et al., 1980). Redoubt has erupted medium-K calc-alkaline basalts, basaltic andesites, andesites, and dacites; andesites are most common (Till et al., 1994). The oldest Pleistocene units erupted ~0.888 Ma and cone-building eruptions were underway by ~0.340 Ma. Dacitic PDC deposits overlie tonalite on the north flank. On the south flank, an exposed dacite dome indicates early effusive activity. Dacitic deposits are overlain by thick sequences of andesitic to basaltic lava flows and block-and-ash-flow deposits. Clay-rich lahar deposits in the surrounding northern, eastern, and southern valleys indicate multiple flank-collapse events (Begét and Nye, 1994; Riehle et al., 1981).

1.2 The 2009 Eruption of Redoubt Volcano

1.2.1 Historical Activity of Redoubt Volcano before 2009

Intermittent observations of Redoubt during the 18th and 19th centuries suggest activity, however, no phenomena can be confidently interpreted as eruptive behavior (Vancouver, 1984). In early 1912, Redoubt erupted explosively, depositing ash over the Cook Inlet (Martin and Katz, 1912). In 1933, Redoubt emitted smoke, though no eruptive products have been linked to this time (Till et al., 1994). In 1966, Redoubt erupted, causing effusive dome growth, PCDs, and removing ~6 x 10^7 m^3 of ice from the upper Drift Glacier (Sturm et al., 1986). The eruption lasted until 1968, with 11 explosive events recorded. Redoubt then erupted over a four-month period during late 1989 through early 1990 resulting in 25 explosions, ash plumes rising 8 – 12 km ASL, pyroclastic flows, 14 emplaced lava domes, and debris flows into the Drift River Valley that destroyed petroleum production and storage facilities (Dorava and Meyer, 1994; Gardner et al., 1994; Miller and Chouet, 1994; Scott and McGimsey, 1994; Trabant et al., 1994; Brantley, 1990).

1.2.2 Overview of the 2009 Eruption

An explosion is called an “Event” and is assigned a sequential number if the Alaska Volcano Observatory (AVO) released a Volcano Activity Notification (VAN) and a Volcano Observatory Notice for Aviation (VONA) following an explosion. During the 2009 eruption of Redoubt Volcano, numbered Events were recorded in association with seismicity detected by seismic station “SPU” located on Mount Spurr, approximately 80 km north of Redoubt (Figure 2). A total of 20 Events were initially identified (Events 0 – 19). Retrospective analysis by McNutt et al. (2013) identified 11 additional Events; however, these are not included in the initial numbering scheme.

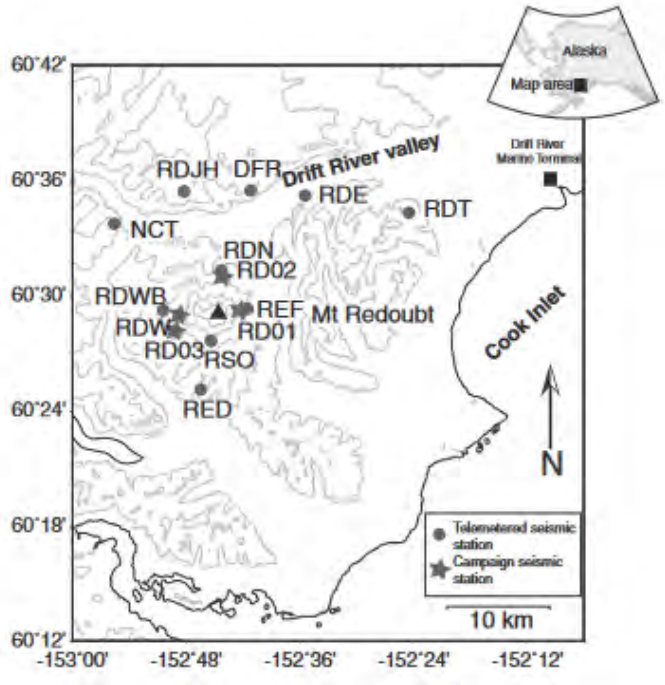

Figure 2: Map of the Redoubt Volcano seismic network operational during the 2009 eruption from Buurman et al. (2013). Stars indicate campaign-style seismometers with onsite recording. Circles indicate telemetered seismic stations set for monitoring during the eruption.

Following Schaefer (2012), Redoubt's eruptive activity is divided here into three "phases": "precursory", "explosive", and "effusive". Pre-eruptive behavior of the precursory phase was first recognized during the summer of 2008 as H_2S emitted from the summit crater (Schaefer, 2012). Elevated CO_2 and H_2S emissions accompanied glacial ice melt below historic vents in the summit crater during the fall of 2008 (Bleick et al., 2013; Werner et al., 2013). Six months prior to the first magmatic explosion on March 23, 2009, the first signals of seismic unrest began as weak volcanic tremors (Figure 3). Approximately 20 deep long-period earthquakes (DLPs; 28 – 41 km below sea level (BSL)) were detected below Redoubt during December of 2008 (Power et al., 2013), suggesting a crustal response to magma movement at depth. Seismicity increased substantially by the end of January 2009, beginning six weeks of volcanic tremors and shallow repeating earthquakes (Buurman et al., 2013) accompanied by high fluxes of CO_2 (Werner et al., 2013). Active magma migration in the upper crust (4 – 6 km) is associated with these phenomena (Bull and Buurman, 2013). A phreatic explosion (Event 0) on March 15 signified the beginning of the explosive phase.

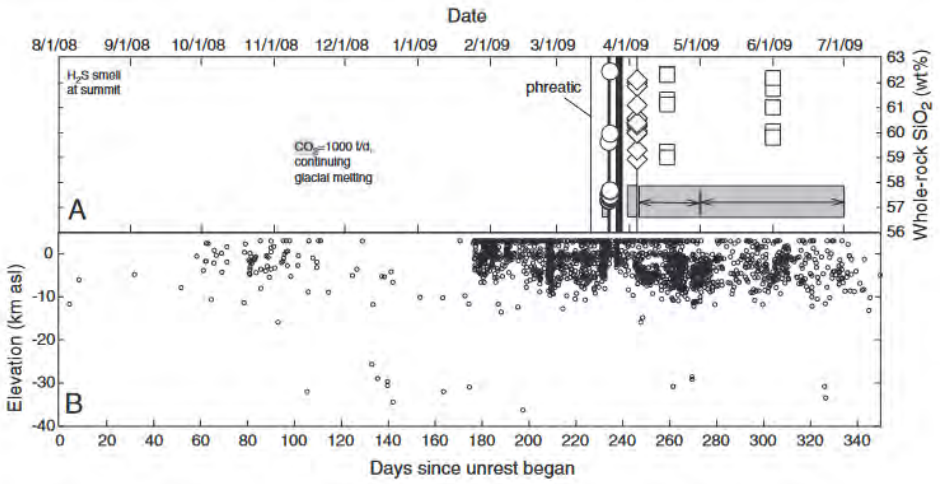

Figure 3: Timeline of the 2009 Redoubt eruption from Coombs et al. (2013). (A) Explosions (vertical lines), lava effusion (gray bars), and whole-rock SiO_2 concentrations from analyzed samples of fall deposits (circles), lahar deposits from the April 4th dome collapse (diamonds), and lava domes (squares). (B) Earthquake hypocenters from Dixon et al. (2010).

The explosive phase occurred from March 15th to April 4th and was characterized by explosions and lava-dome effusion. The highest period of activity began March 23rd and lasted 13 days. More than 19 explosions, several seismic swarms, and intermittent to continuous lava effusion occurred over the explosive phase. Up to three lava domes were produced by effusion and all were destroyed during subsequent explosions. All explosions were likely triggered by conduit overpressure, although Event 19 may have been caused by dome failure (Bull and Buurman, 2013). Events 5 and 6 produced low-, intermediate-, and high-silica andesites (LSA, ISA, and HSA, respectively), while only ISA to HSA were erupted after Event 8 (Coombs et al., 2013). The character of eruptive activity changed after Event 9. Explosions were preceded by repeated episodes of gliding tremors (Buurman et al., 2013; Hotovec et al., 2013); infrasound onsets were impulsive rather than emergent (Fee et al., 2013), and explosions were shorter in duration. Ozone Monitoring Instrument (OMI) and Correlation Spectrometer (COSPEC) SO_2 concentrations increased (Lopez et al., 2013) in addition to increased ejected fine-grained tephra mass (Bull and Buurman, 2013). This change in eruptive behavior has been suggested to relate to changes in erupting magma composition or magmatic storage conditions, as well as an increase in gas over-pressure caused by increased influx of magma to storage areas at depth (Bull and Buurman, 2013). Between Event 18 and 19, explosive activity ceased but active lava effusion and two seismic swarms occurred. The effusion produced the last emplaced lava dome consisting of a dense, degassed magma. Event 19 is thought to have been triggered by dome failure, as is suggested by high gas emission values and explosion plume heights (Bull and Buurman, 2013), though some contribution from conduit overpressure may be involved.

The final, effusive phase began shortly after Event 19 on April 4th with lava effusion initiating growth of the final emplaced dome. Continuous effusion occurred until July 2009, with

changes in eruptive behavior characterized by highly vesicular, P_2O_5-poor lavas (Coombs et al., 2013) in addition to a long-lasting swarm of repeating earthquakes (Buurman et al., 2013). These changes in eruptive behavior are thought to have occurred due to an introduction of evolved ISA to HSA magma in the effusing system (Bull and Buurman, 2013). Total erupted volume of fall, pyroclastic flow, and lava deposits is estimated at 8 – 12 x 10^7 m^3 dense-rock equivalent (DRE) (Buurman et al., 2013). Cumulative CO_2 and SO_2 emissions estimated from airborne and satellite measurements are 2.1 – 2.3 and 1.1 – 1.3 million megatons, respectively (Werner et al., 2013).

Geodetic data retrospectively analyzed by Grapenthin et al. (2013) indicate that magma had risen slowly into the upper crust (10 – 14.5 km) after having risen from 16.5 km as early as May of 2008. Early explosions are consistent with slow ascent and/or shallow storage of magma (Coombs et al., 2013). Additionally, it is suggested that this magma encountered and mixed with bodies of older stalled and differentiated HSA intrusions (Coombs et al., 2013). Over the course of the 2009 eruption, hundreds of flights were cancelled or rerouted, debris fall rendered airports and petroleum facilities inoperable, ash fall forced businesses and city offices to close, and oil production and transportation were disrupted (Schaefer, 2012).

1.2.3 Overview of Events 1 – 6

Events 1 – 6 occurred March 23rd – 24th. Nine explosions occurred during the first two days of activity, producing tephra fall, small PCDs, and multiple lahars. Event 1 produced an ash plume reaching 5.5 km ASL; Events 2 – 6 produced ash plumes reaching 13 – 18 km ASL (Ekstrand et al., 2013; Schneider and Hoblitt, 2013; Wallace et al., 2013). During this period, OMI measured SO_2 levels were >50,000 tons/day (Lopez et al., 2013), while airborne SO_2 and CO_2 levels following Event 6 remained anomalously high (Werner et al., 2013). Infrasound signals occurring during Events 1 – 8 had durations >10 min and emergent onsets (Fee et al., 2013).

Of Events 0 – 6, Events 5 and 6 stand out. Event 5 produced the highest relative acoustic energy (Fee et al., 2013) and highest overall acoustic amplitude (McNutt et al., 2013) recorded during the eruption. High-amplitude tremors followed both explosions (Buurman et al., 2013) and ice-rich lahars inundated the Drift River Valley, flooding the Drift River Terminal (DRT); (Waythomas et al., 2013; Schaefer, 2012). Events 5 and 6 ejected the largest and most vesicular pyroclasts of Events 0 – 19; these pyroclasts consisted of a coarse and highly vesicular scoria with dense clasts. Event 6 produced 15.1 x 10^9 kg of tephra deposits – the highest of Events 0 – 19 (Wallace et al., 2013).

1.2.3.1 A Geophysical Perspective of Events 5 and 6

A weak tremor followed the first phreatic explosion (Event 0) on March 15 (Bleick et al., 2013; Wallace et al., 2013). Seismic swarm "P1" began March 20th and culminated in the first magmatic explosion on March 23rd (Figure 4). This swarm lasted 66 hours and was dominated by repeating earthquakes occurring at depths of 0 – 6 km. These depths are comparable to earthquakes occurring during the 1989 eruption (Ketner and Power, 2013; Power et al., 1994). Spectral analyses of seismic data suggest impulsive P- and S-wave phases likely originated from brittle failure sources during the initial ascent of magma to the surface (Ketner and Power, 2013). Volcanic tremor increased significantly during the final hours of seismic swarm P1, culminating in a 9-hour sequence of six magmatic explosions (Events 1 – 6). A sustained, high-amplitude tremor continued for another 9 hours following Event 6.

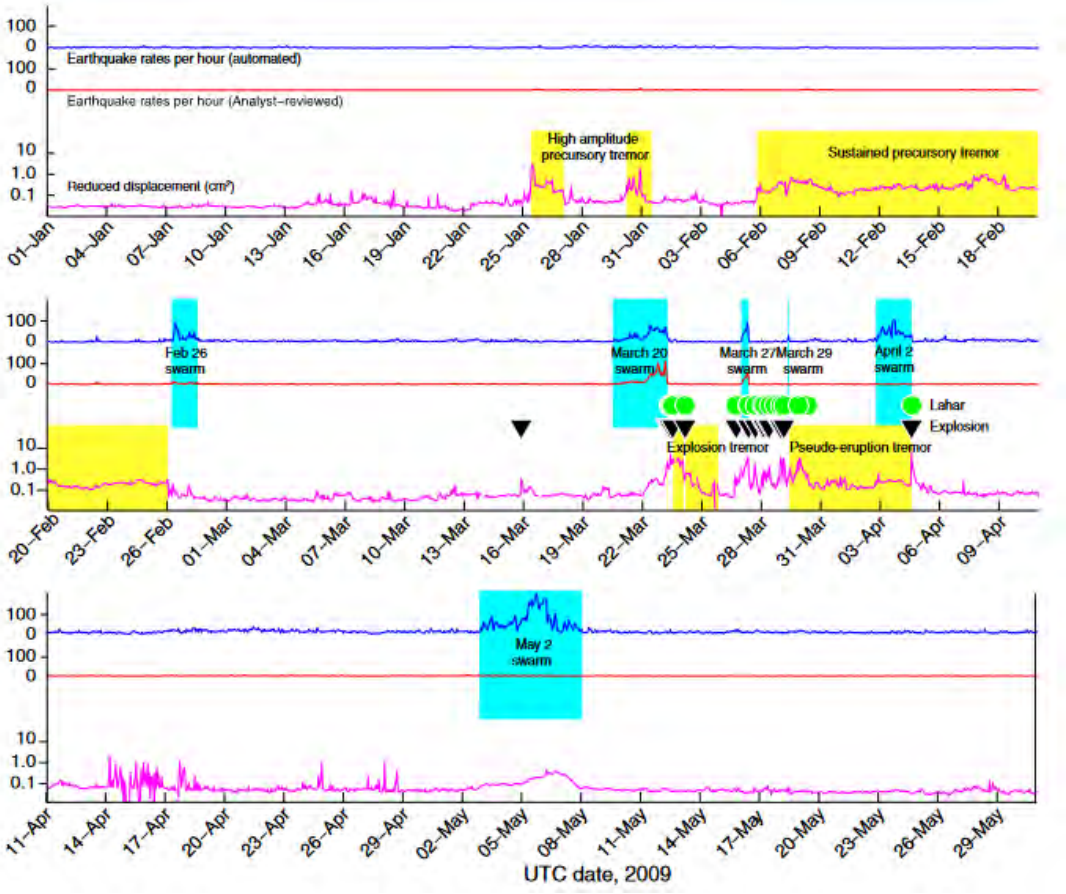

Figure 4: Seismicity associated with the Redoubt eruption (January 1, 2009 – June 1, 2009) from (Buurman et al., 2013). Earthquake rates per hour from the automated catalogue are in blue. Earthquake rates per hour from the analyst-reviewed catalogue are in red. Surface wave reduced displacement (cm^2) is shown in magenta. Six seismic swarm episodes are superimposed in light blue. Significant tremor episodes are superimposed in yellow. Black triangles indicate explosions. Green circles indicate lahars that were generated. Note the March 20th seismic swarm is swarm "P1".

1.2.3.2 A Petrological Perspective of Events 5 and 6

Many vesicular clasts erupted during Events 5 and 6 are crystal-rich LSA (~57.5 wt % SiO_2) and represent the most mafic composition erupted during 2009 (Coombs et al., 2013). Of Events 0 – 6, the most juvenile material was ejected during Events 5 and 6. Phenocryst assemblages were mineralogically uniform, consisting of plagioclase (~An_{70}), FeTi oxides (890 – 960 °C), high-Al amphibole, ortho- and clinopyroxene, and trace magmatic sulfur (Coombs et al., 2013). LSA melt composition was 67 – 68 wt % SiO_2 but ranged to rhyolite with greater microlite growth. This ejecta also contained crystal-rich ISA and HSA (59 – 62.5 wt % SiO_2) with a rhyolitic melt (72 – 74 wt % SiO_2)(Coombs et al., 2013). Later Event ejecta consisted only of ISA to HSA. LSA amphibole phenocrysts have clinopyroxene-rich reaction rims and suggest slow ascent or storage depths where H_2O exsolution could occur. Major and trace element analyses by Coombs et al. (2013) indicate that LSAs and HSAs were produced by in-situ differentiation of earlier Redoubt intrusions, not by fractional crystallization. Clasts of ISA have mixed phenocryst populations and banding textures consistent with formation by mixing of LSA and HSA. Variations in whole-rock trace element versus silica trends suggest multiple HSA magma sources. Major element plagioclase-melt hygrometery of Event 5 and 6 phenocrysts by Coombs et al. (2013) indicate all magma types were stored at 100 – 160 MPa (4 – 6 km depth, 1 – 3 km BSL) assuming the magma was H_2O-saturated. Plagioclase-hosted melt inclusion analyses of Events 5 and 6 phenocrysts by Hosseini et al. (2023) indicate an LSA storage region of 130 – 325 MPa (4.9 – 12.3 km depth) at a temperature of 978 °C. These depths align with the general locus of shallow syn-eruptive seismicity (0 – 3 km) (Schaefer, 2012), pre-eruptive mid-crustal seismicity (3 – 9 km depth) (Power et al., 2013), and tremors occurring in the six-week period leading up to the first eruption (6 – 9 km)(Bull and Buurman, 2013; Buurman et al., 2013).

1.3 Water in Plagioclase Feldspar: Record of Pre-eruptive Magmatic Water and Storage Depths?

In water-rich arc systems, magmas are generally stored at depths where they become water saturated (Rasmussen et al., 2022). As magma follows a known water saturation curve with depth, pre-eruptive water content of a magma may be used to infer approximate magma storage depths preceding eruption (Figure 5). Recent work has shown that nominally anhydrous minerals (NAMs) may be used as hygrometers, i.e., they may be used to estimate the water contents of their host magmas (Urann et al., 2022). Nominally anhydrous minerals refer to minerals with chemical formulae written without hydrogen, though they may contain trace amounts of hydrous components (Libowitzky and Beran, 2006; Bell and Rossman, 1992; Soloman and Rossman, 1988).

Pre-eruptive magmatic water contents are difficult to constrain as water degasses from magma during ascent, meaning information about the initial water content of a magma is lost. Magma may be trapped in minerals as melt inclusions, reducing degassing during ascent. Analyses of H_2O and CO_2 in melt inclusions have been used to infer pre-eruptive magma storage depths (Wallace et al., 2021; Plank et al., 2013; Wallace, 2005), though difficult sample preparation and post-entrapment processes complicate interpretation (Rasmussen et al., 2022; Rose-Koga et al., 2021; Voyer et al., 2014; Bucholz et al., 2013). Additionally, while melt hygrometry has been applied using olivine crystals (Newcombe et al., 2020; Peslier et al., 2015; Demouchy et al., 2006; Peslier and Luhr, 2006), olivine is uncommon in dacitic to rhyolitic systems. Mineral phases common to silica-rich systems, such as plagioclase feldspar $(Ca,Na)[Al(Al,Si)Si_2O_8]$, may be potential hygrometers. Volcanic plagioclase is prevalent in all common magma compositions, has been found to contain water in the 10s to 100s ppm (Caseres et al., 2018; Hamada et al., 2011; Seaman et al., 2006; Johnson and Rossman, 2004), and has been used to constrain the water contents of their host melts (Caseres et al., 2018; Hamada et al., 2013). Measuring water in plagioclase may provide a complementary, easy-to-measure record of pre-eruptive water contents that can be used to estimate pre-eruptive magma storage depths in water-rich systems.

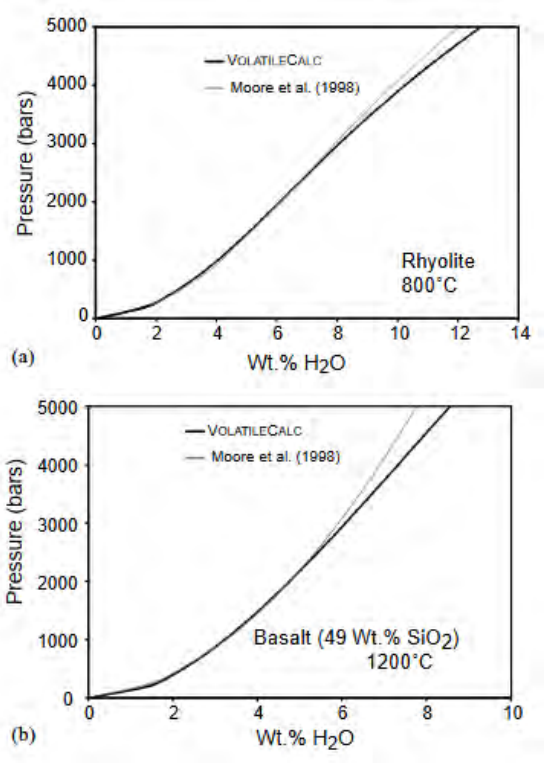

Figure 5: H_2O solubility as a function of pressure in rhyolitic and basaltic melts as calculated by VolatileCalc from Newman and Lowenstern (2002) compared with the Moore et al. (1998). (a) Comparison of rhyolite Solubility versus Pressure in VolatileCalc at 800°C and a CAM-73 rhyolite composition from Moore et al. (1998). (b) Comparison of basalt Solubility versus Pressure in VolatileCalc at 1200°C and a "Kilauea Tholeiite" composition from Dixon (1997) run through Moore et al. (1998).

Hydrogen (H) in feldspar is colloquially referred to as “water” and is calculated as H_2O. However, H may not solely dissolve as molecular water (H_2O_m). Water has been detected as hydroxyl (OH^-) and ammonium (NH_4^+) in igneous feldspars (Behrens, 2021; Johnson and Rossman, 2004, 2003) and so far, only OH^- has been detected in volcanic plagioclase (Behrens, 2021; Johnson and Rossman, 2004). Water in volcanic plagioclase has been measured using Fourier Transform Infrared Spectroscopy (FTIR) (Behrens, 2021; Mosenfelder et al., 2015; Hamada et al., 2013; Johnson and Rossman, 2003).

A plagioclase-melt partition coefficient is needed to calculate melt water concentrations using the Beer-Lambert Law. The plagioclase-melt partition coefficient is the ratio of water concentration in a plagioclase phenocryst and its host melt at equilibrium. Plagioclase-melt partition coefficients have been determined in experimental studies where changes in conditions (e.g., pressure, temperature, oxygen fugacity, melt composition, and mineral composition) affect the partitioning behavior (Yang, 2012). Coefficient values for plagioclase-melt systems range from 0.002 to 0.005 (Mosenfelder et al., 2020). As water is present in plagioclase in trace amounts (≤ 100 wt ppm water in plagioclase, ≤ 1 wt% H_2O in melt), a constant partition coefficient can be applied (Hamada et al., 2013). A partition coefficient of 0.002 has been estimated for dacitic to rhyolitic systems (Rappoccio et al., 2020; Caseres et al., 2018; Mosenfelder et al., 2018). The 0.002 value will be used in this study.

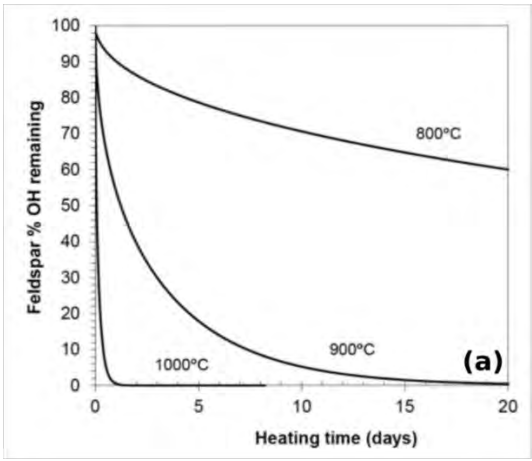

Figure 6: Diffusion model from Johnson and Rossman (2013) of OH^- concentration remaining in a spherical feldspar grain with a diameter 1 mm as a function of time at 800, 900, and 1000°C using Equation 6.20, p.91, of Crank, (1975) for diffusion in a solid sphere.

The ability of plagioclase to provide a record of pre-eruptive water concentration depends on the diffusive speed of water in plagioclase. Water diffusion experiments and modeling performed on plagioclase between 800 - 1000°C (Johnson and Rossman, 2013) indicate diffusive re-equilibration of water in an idealized spherical andesine plagioclase crystal of 1 mm diameter between 1 and 20 days at 1000°C and 900°C, respectively (Figure 6). This means water concentrations (and by proxy, depths) may be overprinted during magma ascent and stalling as equilibration of water between the plagioclase and the melt occurs.

2. Motivation

2.1 Volcanic Hazard and Mitigation

Volcanic eruptions typically occur over hours to weeks, but may occur over years, and are usually preceded by a preparatory phase wherein one or more magma reservoirs are recharged. Volcanoes vary in eruption frequency; some may erupt continuously or frequently while others may remain dormant for thousands of years between eruptions. Additionally, volcanoes vary in eruption style; they may erupt effusively or explosively, and the eruption style may change over time. The duration and impact of eruptions are also variable; an eruption may last minutes and only impact areas immediately surrounding the volcanic vent, or it may have global impacts lasting years to decades. Eruptions can cause considerable damage and disruption to human populations and important economic networks (Cioni et al., 2014).

Geophysical monitoring systems are primarily used to inform eruption forecasts (Marzocchi and Bebbington, 2012; Sparks and Aspinall, 2004). Most eruptions are preceded by weeks to months of volcanic unrest. Increases in the rate of seismicity, crustal deformation, and degassing signal volcanic unrest. Based on these signals, observatories may issue warnings of impending eruptions. Short-term forecasts are currently informed by monitoring signals, geologic history (e.g., past eruptive behavior and the distribution of past eruption deposits), volcanic structure, and scientific models linking magma ascent rate to unrest signals. However, the unrest period is variable. Eruptions may occur without detectable precursor signals (e.g., Ogiso et al. (2015)) or signals may last years before an eruption occurs. Improvements in all aspects of volcanic hazard mitigation, including monitoring networks, long- and short-term forecasting (Poland & Anderson, 2020; Marzocchi & Bebbington, 2012), hazard assessment (Wadge and Aspinall, 2014), and education (Leonard et al., 2014; Lindsay et al., 2010; Solana et al., 2008) have reduced fatalities.

Accurate eruption forecasting remains a challenge, even in well-monitored volcanic systems. Pre-eruptive geophysical observations understood within a post-eruptive petrologic context may help inform future forecasting efforts by tying pattern recognition to a more mechanistic understanding of magma storage and migration in volcanic systems. Several studies have demonstrated correspondence between petrologic timescales and eruption precursors (Rasmussen et al., 2018; Ruth et al., 2018; Saunders et al., 2012; Kahl et al., 2011). However, current petrologic tools constraining hour to month timescales of pre-eruptive magma migration lack the depth resolution useful in interpreting seismic signals trough time and space. Water in plagioclase feldspar has potential as a hygrometer and barometer and could potentially track magma migration in the hours to month prior to eruption.

2.2 Redoubt Volcano and Broader Implications

Nominally anhydrous minerals may provide important insights into the study of water behavior in magmatic systems. The abundance of plagioclase feldspar in intermediate magmas suggests that plagioclase could be an easily accessible and useful recorder of magmatic volatiles. However, there are very few studies of water in volcanic feldspars (Mosenfelder et al., 2020; Hamada et al., 2013; Johnson & Rossman, 2003, 2004) and in varying volcanic systems (Castilla Montagut, 2022; Caseres, 2019; Hamada et al., 2011). The proposed work will contribute plagioclase water concentration and pre-eruptive storage depth data from an additional volcanic system. The 2009 eruption of Redoubt Volcano is well documented, covering multiple fields – geodesy, seismology, volcanology, and petrology. This is a promising system to evaluate the potential of plagioclase as a hygrometer and barometer.

2.3 Statement of Purpose

This project will use water in plagioclase to estimate pre-eruptive magma storage depths of two 2009 Redoubt eruption events and compare these depths to estimations indicated by the seismic record preceding eruption. Measured water concentrations will be used to calculate magma storage depth. Depths will then be compared against existing plagioclase-melt hygrometry (Coombs et al., 2013) and melt inclusion (Hosseini et al., 2023) analyses, and epicenter depths calculated for seismic precursor events (Ketner and Power, 2013) occurring in the days prior to eruption.

2.4 Hypothesis

Null Hypothesis: There is no relationship between storage depths calculated using water-in-plagioclase and storage depths estimated from plagioclase-melt hygrometry and pre-eruptive earthquake hypocenter depths.

Alternative Hypothesis: Storage depths calculated from water-in-plagioclase will overlap within uncertainty with existing storage depths estimated from plagioclase-melt hygrometry and pre-eruptive earthquake hypocenter depths. *

*Caveat: If ascent occurred within the diffusional recording time of H in plagioclase (i.e., H signatures from pre-eruptive storage at saturation pressure have not been completely overprinted by re-equilibration with a degassed or degassing melt).

3. Methods

3.1 Sample Preparation

Pyroclasts from Event 5 and Event 6 were provided by the Alaska Volcano Observatory (AVO). Ten total clasts, five from Event 5 and five from Event 6 were lightly crushed and sieved. One plagioclase phenocryst from each clast was collected using tweezers and a Leica S9i Stereomicroscope. The phenocrysts were immersed in isopropanol to screen for cracks, melt inclusions, and melt re-entrants. Due to difficult sample preparation phenocrysts were prepared by two methods. In the first method, grains were mounted in either dental resin or crystalbond and polished on two parallel sides down to a grit of 0.3 µm. In the second method, phenocrysts were mounted in a one-inch round of dental resin, then cut in half with a Princeton Scientific WS 25 Wire Saw using a 20 µm titanium wire and a glycerol-boron-carbide slurry. One-half of each one-inch round was then oriented perpendicular to horizontal and imbedded in a separate one-inch round of dental resin (Figure 7). Each phenocryst half was then polished to a slab with grits down to 0.3 µm.

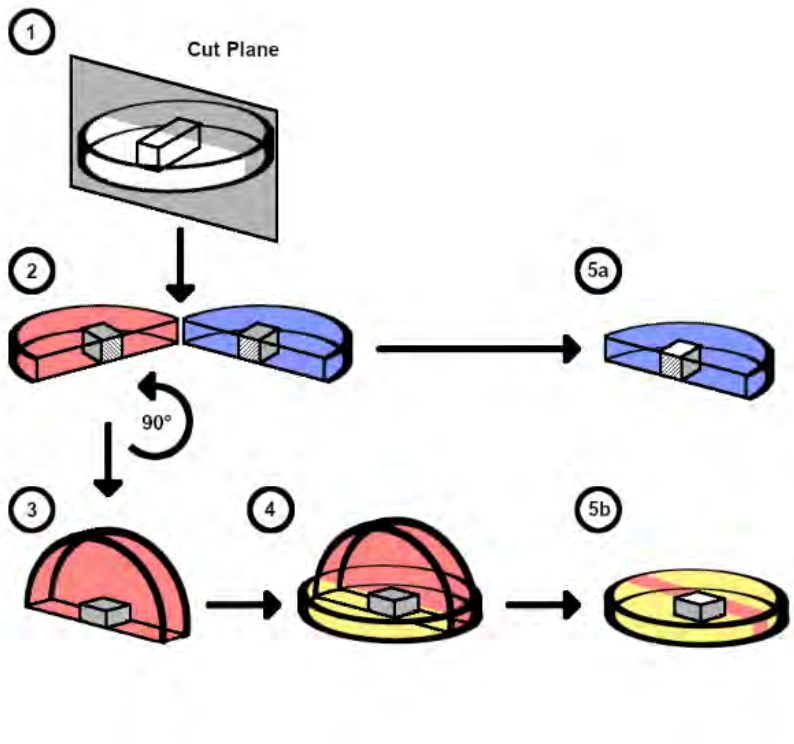

Figure 7: Sample preparation following Method 2. (1) Plagioclase grain is mounted in a dental resin puck. The puck is then cut in half (gray plane) on the wire saw. (2) One half of the puck (blue) is left in its original orientation, while the second half (red) is rotated. (3) The second half of the puck (red) is rotated 90 degrees vertically. (4) The rotated half is mounted in another dental resin puck. (5a and 5b) Both halves are polished, accounting for three mutually perpendicular directions.

Phenocrysts are cut and oriented as described above because accurate quantification of absolute water concentration by FTIR requires the integration of OH^-absorption peaks in three perpendicular directions. The orientation scheme means each phenocryst half will account for two of three mutually perpendicular axes (e.g., half one will have axes X and Z while half two will have axes X and Y). Additionally, this method preserves the rims of the feldspars, where water concentration gradients are expected to be preserved if these samples are revisited for diffusion chronometry. This technique has been successfully tested at UMD in previous research (Castilla Montagut, 2022). Single slabs, while easier to prepare, cannot be measured for a third axis (see Section 3.3 for more information).

Samples were then cleaned to remove organic contaminants from the dental resin or Crystalbond. The samples were first soaked in acetone for 24 hours to remove most of the resin. Samples were then sonicated in a DK SONIC Digital Ultrasonic Cleaner; 3 x 30 minutes in acetone, toluene, and isopropanol, in that order.

3.2 Fourier Transform Infrared Spectroscopy

Fourier transform infrared spectroscopy (FTIR) is a technique where an infrared spectrum of emission or absorption is obtained for a solid, liquid, or gas. A spectrum is composed of peaks associated with an analyzed sample's chemical constituents and their abundances. The absorption of certain IR wavelengths corresponds to vibrational bond energies of functional groups like OH^-.

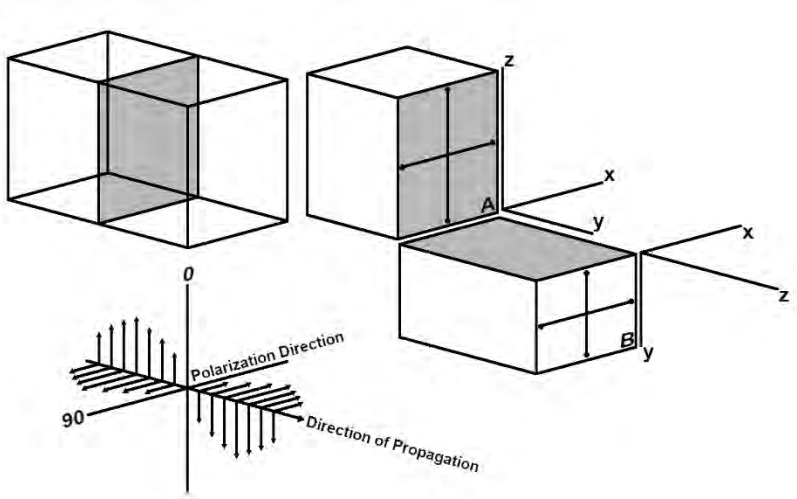

Figure 8: Pictorial representation of measuring water concentration in a plagioclase crystal by FTIR. A plagioclase phenocryst is cut in half. Each half accounting for two of three axes (e.g., X – Z and X – Y) is polished on two parallel sides. The crosses present on faces A and B represent profiles along which measurements are taken. Polarized light (0° and 90°) will be transmitted perpendicular to the faces A and B, allowing for measurement of individual axial spectra (e.g., polarized light at 0° on face A will measure the spectral signal along axis Z only). X, Y, and Z denote crystallographic axes, but water concentration may be quantified using light polarized in any three mutually perpendicular directions, so it is not necessary to exactly align the slabs with the crystallographic axes. Modified after Figure 8 in Castilla Montagut (2022).

Transmission spectra of polished plagioclase crystals were obtained using a Thermo Scientific Nicolet iN10 MX Fourier Transform Infrared Spectrometer with a N_2-cooled MCT detector at the University of Maryland Planetary Volcanism Laboratory. Samples were measured on a KBr salt plate. The sample and surroundings were continuously purged with dry, CO_2-free air to eliminate atmospheric CO_2 contributions to spectra. The background and sample spectra (600 – 6000 cm^{-1}) were taken with the following settings: 256 scans at 4 cm^{-1} resolution and a 50 x 50 μm aperture size. Transmission spectra polarized at 0° and 90° were obtained for all measurements, accounting for spectral contributions on three mutually perpendicular directions (Figure 8). A single spot analysis was taken on each crystal in a spot clear of cracks and inclusions. Using OMNIC Picta software, the area under the spectral curve associated with OH^- in plagioclase (3700 – 2600 cm^{-1}) was calculated and used to estimate water concentration.

3.3 Hygrometry: The Beer-Lambert Law and Calculating the Concentration of Water in the Melt

Water concentration at every point in a profile was calculated using the Beer-Lambert Law (Eq. 1):

$$C = \frac{(mw)(A)}{\rho * d * \varepsilon} \quad (1)$$

Where *C* is the concentration of the absorbing species (wt %); *mw* is the molecular weight of the species ($g \cdot mol^{-1}$), *A* is the absorbance peak area (cm^{-1}), ρ is the density of the sample ($g \cdot L^{-1}$), *d* is the sample thickness (cm), and ε is the molar absorption coefficient ($L \cdot mol^{-1} \cdot cm^{-2}$).

The species of interest in this study is H_2O, meaning *mw* is 18.02 $g \cdot mol^{-1}$. Absorbance peak area *A* was calculated using OMNIC Picta software. This software integrates the area under the spectral curve between two specified wave numbers, then subtracts a baseline area specified by a linear path between the same two wave numbers to estimate the spectral absorbance contribution of OH^-. The density of the sample was assumed to be 2650 $g \cdot L^{-1}$ (Mosenfelder et al., 2015). The crystal thickness *d* was measured using a Mitutoyo micrometer. The molar absorption coefficient ε is 202600 ± 20260 $L \cdot mol^{-1}$ $H_2O \cdot cm^{-2}$ (Mosenfelder et al., 2015).

Calculated water concentration is determined from the sum of areas of three mutually perpendicular spectral directions. In this study, three methods for determining peak area were used to account for the number of measurable axes. Method 1 was used for grains that had been cut and polished in two slabs and is calculated following Eq.(2) where A is absorbance (cm^{-1}). Method 2 and Method 3 were used for single polished slabs. Method 2

assumes equal spectral contribution from all three axes and is calculated following Eq.(3). Method 3 assumes one axis is spectrally dominant and the remaining two axes contribute less than the first axis, are about equal in spectral contribution, and is calculated following Eq.(4). It is important to note that given a significant diffusion profile, FTIR will underestimate the amount of H_2O for any thickness of plagioclase.

Method 1 $$A_{tot} = A_x + A_y + A_z \quad (2)$$

Method 2 $$A_{tot} = \frac{3}{2}(A_x + A_y) \quad (3)$$

Method 3 $$A_{tot} = A_x + 2A_y \quad (4)$$

Concentration of water in the crystal may then be related to the concentration of water in the melt Eq.(5):

$$C_{melt\ (wt.\%)} = \frac{C_{crystal\ (wt.\%)}}{K_d} \quad (5)$$

where K_d is the plagioclase-melt partition coefficient (0.002 in this study). Confining pressure was then calculated using VolatileCalc.

3.4 VolatileCalc: Calculating Confining Pressure

VolatileCalc is a solubility model for system melt–H_2O–CO_2 developed by Newman and Lowenstern, (2002), and runs in Microsoft Excel. The VolatileCalc Saturation Pressure macro calculates the system confining pressure using water concentration. This macro calculates the pressure at which a silicate melt of known dissolved H_2O and CO_2 concentrations would be saturated with a vapor phase, as well as the composition of the vapor in equilibrium with that melt. VolatileCalc assumes the following for its calculations:

> H_2O and CO_2 mix ideally within the vapor phase; volume and enthalpy are constant over the pressure and temperature ranges of interest (0 – 5000 bar and 600 - 1500°C, respectively); Henrian behavior for the solubility of a volatile gas in the melt (i.e., H_2O dilutes linearly in the vapor phase as concentration decreases in the melt); H_2O solubility in a silicate melt is independent of CO_2 concentration, and vice versa (this applies to low pressures < 4000 bars (Blank et al., 1993) but may not be valid for pressures > 4000 bars (Jakobsson, 1997; Mysen et al., 1976)).

Due to restrictions in system composition inputs (rhyolitic vs. basaltic), the basalt H_2O-CO_2 code was used to approximate the Redoubt system. Calculation inputs include H_2O (wt %) and CO_2 (ppm) in the melt (relative to the melt and dissolved volatiles but not to crystals), and temperature (°C). The program outputs H_2O speciation as mol H_2O_m and OH^-, vapor composition in mol% H_2O and CO_2, and importantly, pressure in bars.

3.5 Pre-eruptive Storage Depth Calculation

The pressure calculation using VolatileCalc may then be used to roughly estimate a depth Eq.(6):

$$P = \rho g h \tag{6}$$

where *P* is pressure (Pa), ρ is crustal density (2830 kg/m^3) (Christensen and Mooney, 1995), *g* is gravity (9.8 m/s^2), and *h* is depth (m).

3.6 Uncertainties

The following section attempts to constrain, or at least address, sources of uncertainty to calculated magma water contents and storage depths, though it is recognized that this discussion is by no means exhaustive. Table 1 presents a generalized list of uncertainty sources and error types associated with each step of the analytical protocol.

3.6.1 Uncertainties in Calculating Water Concentration in Plagioclase

Calculating water concentration in plagioclase by FTIR spectroscopy is based on the principle that absolute water concentration is related to the area under the spectral curve associated with OH^-. This subsection will attempt to cover uncertainties in area selection and concentration calculation.

3.6.1.1 Manual Baseline Determination and Area Calculation

One component to calculating the area under the curve is the selection of a baseline from which the background is subtracted and the spectral contribution of OH^- may be determined. Baselines may be linear or non-linear; this study used a linear baseline. The main complication with respect to uncertainty is that baselines are often manually determined (Jirasek et al., 2004). Additionally, the OH^- peak position in a plagioclase infrared spectrum is variable, and the center of this peak may shift by a few wavenumbers in either direction (Johnson and Rossman, 2004). In addition to these factors, there is no

Table 1: Table of generalized uncertainty sources associated with each step of the analytical protocol.

Sources of Uncertainty	
Analytical step	Error type
Pyroclastic crushing and grain picking	Possible loss of spatial data only, could be systematic
Cutting, polishing, and cleaning	Systematic
FTIR spectrometry – molar Absorption Coefficient	Systematic
FTIR spectrometry - plagioclase density	Systematic
FTIR spectrometry - grain thickness	Random
FTIR spectrometry - unpolarized measurements	Systematic
FTIR spectrometry - error from repeated analyses	Random
FTIR spectrometry - baseline selection	Systematic
Hygrometry – K_d	Systematic
VolatileCalc - input H_2O	Systematic
VolatileCalc - input CO_2	Systematic
VolatileCalc - input SiO_2	Systematic
VolatileCalc - input T	Systematic
Depth calculation - crustal density	Systematic

existing standard for baseline picks. As such the total area under the curve selected may vary, resulting in calculated water concentrations varying by 10s of ppm.

In this study, a “more conservative” and “less conservative” area was selected for each point in a traverse to attempt to constrain water concentration and investigate the influence of area picks on calculated water concentration (Figure 9). Boundaries were

selected by the following criteria: for the more conservative estimations, the right lower bound (LB) baseline point was always put at 2800 cm^{-1}, at the extent of O – H stretching vibration for both molecular water and OH^-, and the left upper bound (UB) was placed towards the saddle of the left side of the OH^- peak. For the less conservative estimations, the UB was placed such that it generally followed the shape of the Fe stretching bonds to the left of the OH^- peak, while the LB was placed as far to the right as possible without subtracting area through integration (this represents a physically impossible system).

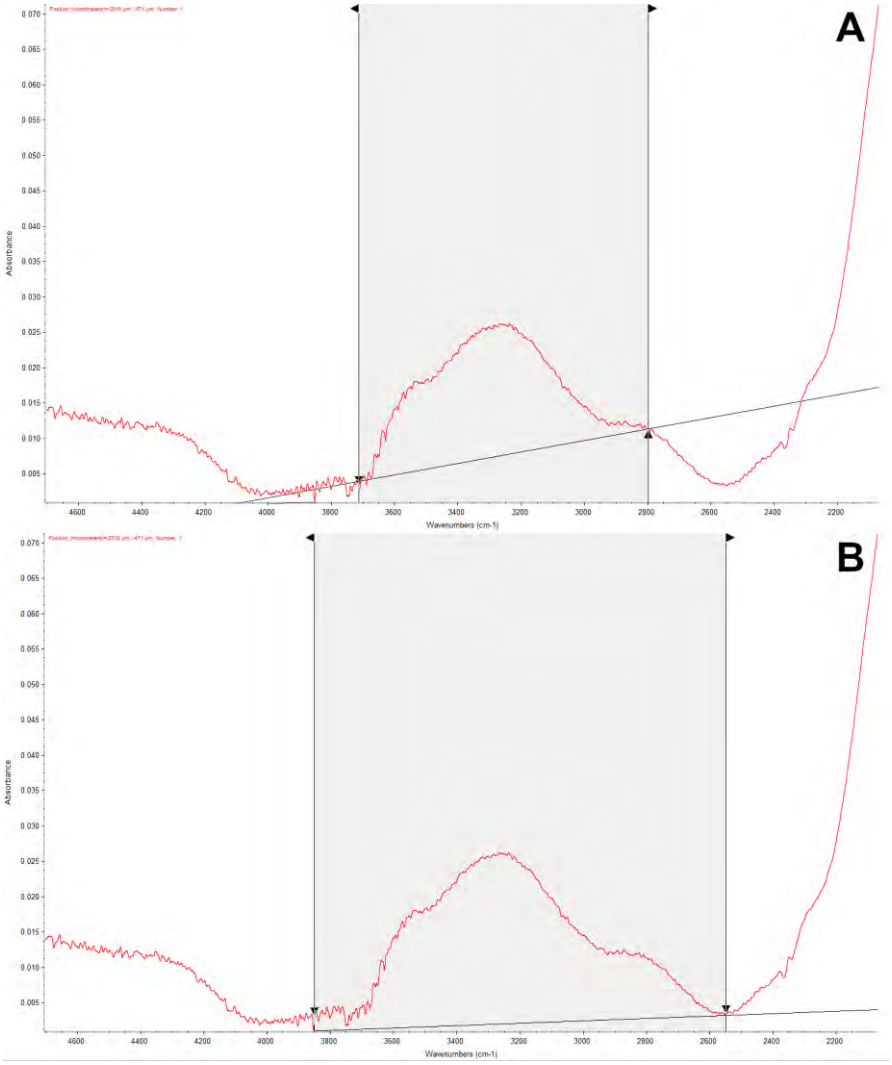

Figure 9: Example of area calculation of OH^- peak in sample RED09 – E5C1 – X1. Two different linear baselines are used to produce a (A) conservative lower (8.9 cm^{-1}) and (B) upper (15.3 cm^{-1}) bound on the peak area corresponding to the O – H bond.

Concentration results are then presented as a plot with two concentrations at every traverse point, along with their associated uncertainties (Figure 10).

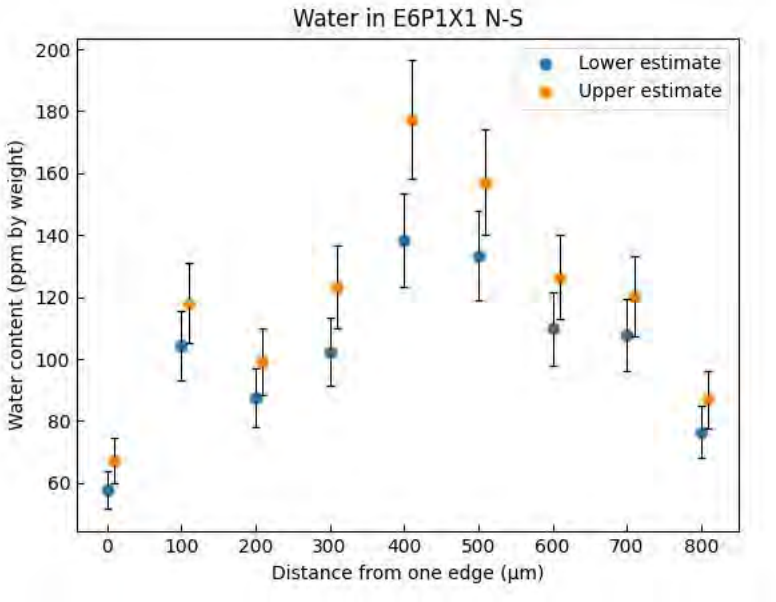

Figure 10: Example of calculated water concentrations calculated from a traverse across a single grain with several unpolarized spot measurements and uncertainty (1σ) from known sources of error (thickness and absorption coefficient). This figure is mainly for illustrative purposes to demonstrate the bracketing method for concentration calculations. This study did not take traverses across grains. Rather, one spot measurement per sample was taken. Upper estimate datapoints offset by 10 μm from their actual position for clarity.

Uncertainties introduced by instrumentation were also considered. Three spectra, following the protocol established in Section 3.2, were taken on a single point on sample RED09E6P1X1. The same baseline to calculate area was applied to all three spectra. Integrated absolute absorbance from these three spectra were averaged and standard deviations of those measurements were taken. It was found that uncertainty in calculated water concentration varied by as much as ~0.26 ppm even if baseline is kept consistent. This implies that lower water concentration will have a higher relative uncertainty, and in the case of concentration gradients being present in a phenocryst, uncertainty will increase from the center of the grain where concentrations are highest to the edge of the grain where concentrations are lowest. Comparisons between the uncertainties with manual baseline picks and instrumentation have not been fully assessed. It is assumed that for sufficiently high concentrations, instrumentation uncertainties are negligible compared to uncertainties arising from baseline picks and so have not been considered in the uncertainties of the preliminary results.

3.6.1.2 Uncertainties using the Beer-Lambert Law

The Beer-Lambert Law consists of five input variables: molecular weight (*mw*), peak area (*A*), sample density (ρ), sample thickness (*d*), and the molar absorption coefficient of plagioclase (ε). A compiled list of uncertainties can be found in Table 2.

Table 2: Compiled table of uncertainties of variables in the Beer-Lambert equation.

Beer-Lambert Law Uncertainties Table		
Variable	Value	Uncertainty
mw	18.015 g · mol^{-1}	± 0 g · mol^{-1} This value is assumed to have no uncertainty.
A	Variable	Variable Uncertainties created by manual baseline selection exceed variabilities in instrumentation (Jirasek et al., 2004). Assessment of uncertainties relevant to this study are ongoing.
ρ	2650 g · L^{-1} This value was assumed by Mosenfelder et al. (2015) in the determination of *ε*.	± 0 g · L^{-1} An evaluation of uncertainty would introduce several layers of complexity that would take considerable time to address. For simplicity, this value is assumed to have no uncertainty, though the density of plagioclase is variable
d	Variable At least three measurements from a Mitutoyo micrometer will be taken and averaged.	Variable The uncertainty will be determined through the standard deviation of all measurements averaged.
ε	202600 L · mol^{-1} H_2O · cm^{-2}	± 20260 L · mol^{-1} H_2O · cm^{-2} Mosenfelder et al. (2015) provides a ± 10% uncertainty to *ε,* though it is unclear how this number was derived.

3.6.1.3 Error Equations used in the Calculation of Water Concentration

Multiplication

$$E_{product} = \sqrt{(E_A B)^2 + (E_B A)^2} \quad (7)$$

Division

$$E_{quotient} = \left(\frac{1}{B^2}\right)\sqrt{(E_A B)^2 + (E_B A)^2} \quad (8)$$

3.6.2 VolatileCalc and Depth Calculation

This study has not investigated uncertainties and assumptions present in the construction of VolatileCalc macros. Operating under the assumption that the depth can be no more accurate than the largest uncertainty used to calculate it, the depth uncertainty is at least ± 30% (a conservative estimate of error introduced by manual baseline picks following Koga et al. (2003), Peslier and Luhr (2006); Rossman (2006).

4. Results

In total, eleven crystals were analyzed; three from Event 5 and eight from Event 6. Due to the meticulous nature of sample preparation, and multiple possible avenues of sample degradation during the process, only one crystal (E5C4 – X1) was successfully cut, polished, cleaned, and analyzed. The remaining ten crystals were prepared as single slabs, doubly polished on two parallel sides. Every crystal analyzed contained many cracks and inclusions; FTIR analysis spots relatively clear of these features were uncommon. Because of this, only one spot was analyzed per crystal. Calculated plagioclase H_2O concentrations and estimated depths are given in Table 3. Plotted plagioclase H_2O concentrations are shown in Figure 11. Complied estimations of magma storage and migration depths along with study sample depths are shown in Figure 12.

Table 3: Table of plagioclase H_2O concentrations and calculated depths with upper and lower estimates noted as a range.

Sample	Plagioclase H_2O (ppm) (Method 1)*	Plagioclase H_2O (ppm) (Method 2)†	Plagioclase H_2O (ppm) (Method 3)‡	Estimated Depth (km)
E5C1 – X1	-	13 ± 4 – 18 ± 5	12 ± 4 – 16 ± 5	0.12 ± 0.04 – 0.28 ± 0.08
E5C2 – X1	-	175 ± 53 – 231 ± 69	158 ± 47 – 211 ± 63	22 ± 7 – ≥ 34§
E5C4 – X1 – H1	135 ± 41 – 174 ± 52	136 ± 41 – 180 ± 54	133 ± 40 – 174 ± 52	17 ± 5 – 27 ± 8
E5C4 – X1 – H2	144 ± 43 – 192 ± 58	153 ± 46 – 206 ± 62	146 ± 44 – 192 ± 58	19 ± 6 – 31 ± 9
E6C1 – X1	-	657 ± 197 – 1165 ± 350	649 ± 195 – 1124 ± 337	> 34§
E6C1 – X2	-	366 ± 110 – 443 ± 133	361 ± 108 – 434 ± 130	> 34§
E6C1 – X3	-	152 ± 46 – 261 ± 78	129 ± 39 – 248 ± 74	16 ± 5 – > 34§
E6C1 – X4	-	280 ± 84 – 357 ± 107	263 ± 79 – 336 ± 101	> 34§
E6C1 – X5	-	413 ± 124 – 601 ± 180	397 ± 119 – 583 ± 175	> 34§
E6C1 – X6	-	369 ± 111 – 619 ± 186	296 ± 89 – 539 ± 162	> 34§
E6C1 – X7	-	335 ± 101 – 746 ± 224	301 ± 90 – 589 ± 177	> 34§
E6C2 – X1	-	137 ± 41 – 177 ± 53	128 ± 38 – 167 ± 50	16 ± 5 – 26 ± 8

* $A_{tot} = A_x + A_y + A_z$ where A is absorbance (cm^{-1})

† $A_{tot} = (3/2) * (A_x + A_y)$

‡ $A_{tot} = A_x + 2A_y$ where $A_x > A_y$

§ Calculated wt % H_2O in the melt exceeds the 11 wt % maximum input limit of VolatileCalc

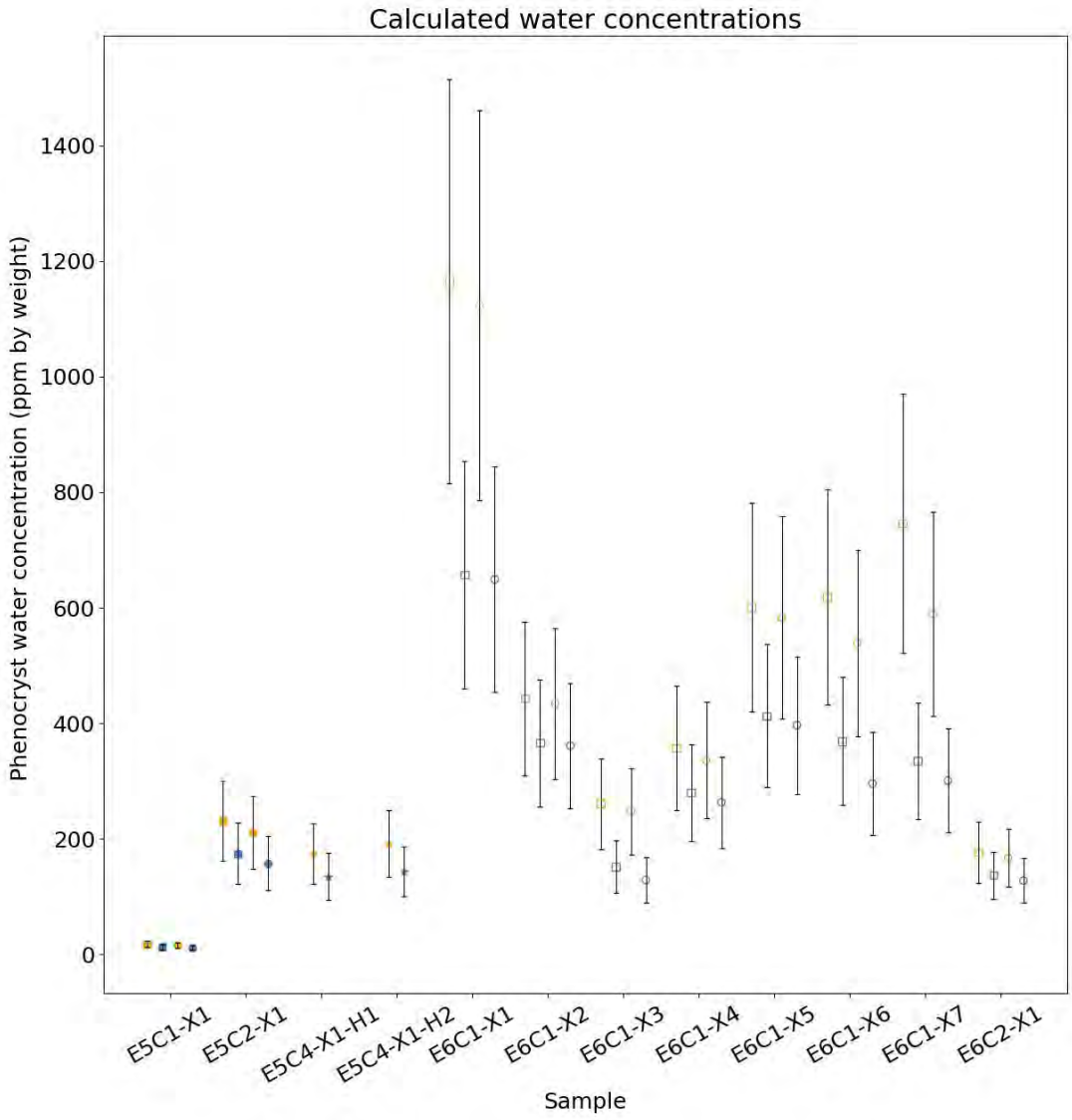

Figure 11: Plotted calculated water concentrations from spot analyses in plagioclase samples. Orange symbols represent upper estimates. Blue symbols represent lower estimates. Solid symbols represent Event 5 samples. Open symbols represent Event 6 samples. Stars are concentrations calculated using areas determined by Method 1. Squares are concentrations calculated using areas determined by Method 2. Circles are concentrations calculated using areas determined by Method 3. The uncertainty for every sample is ± 30 %.

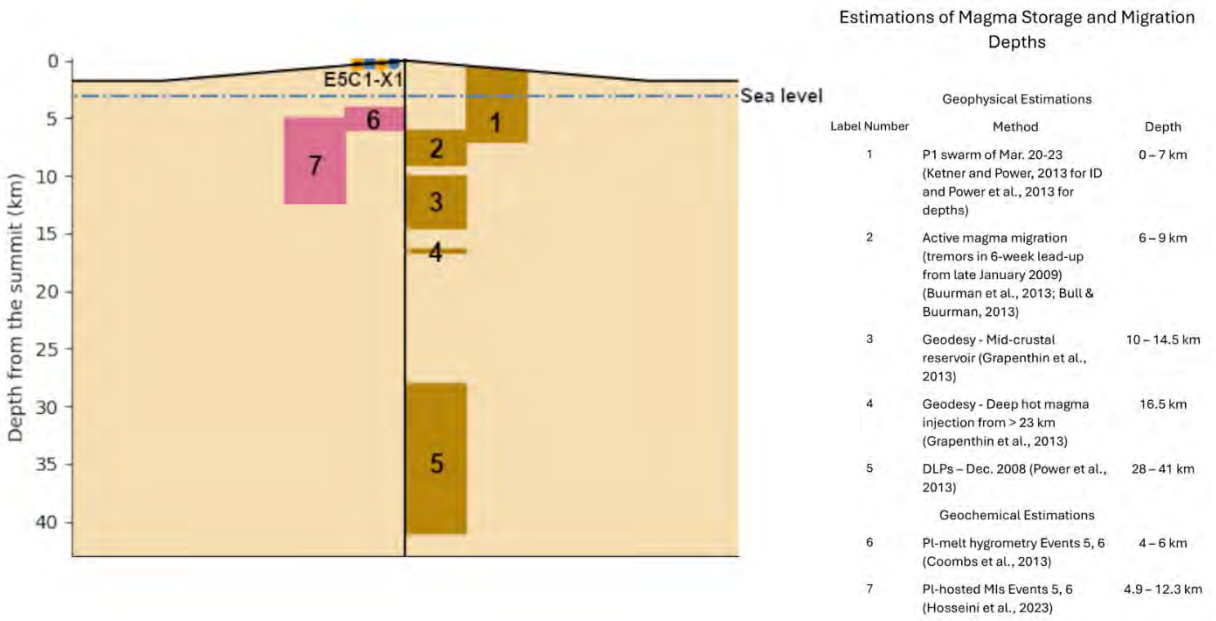

Estimations of Magma Storage and Migration Depths

Label Number	Method	Depth
	Geophysical Estimations	
1	P1 swarm of Mar. 20-23 (Ketner and Power, 2013 for ID and Power et al., 2013 for depths)	0 – 7 km
2	Active magma migration (tremors in 6-week lead-up from late January 2009) (Buurman et al., 2013; Bull & Buurman, 2013)	6 – 9 km
3	Geodesy - Mid-crustal reservoir (Grapenthin et al., 2013)	10 – 14.5 km
4	Geodesy - Deep hot magma injection from > 23 km (Grapenthin et al., 2013)	16.5 km
5	DLPs – Dec. 2008 (Power et al., 2013)	28 – 41 km
	Geochemical Estimations	
6	Pl-melt hygrometry Events 5, 6 (Coombs et al., 2013)	4 – 6 km
7	Pl-hosted MIs Events 5, 6 (Hosseini et al., 2023)	4.9 – 12.3 km

Figure 12: Complied estimations of magma storage and migration depths. Brown shaded regions indicate geophysical estimations. Purple shaded regions indicate geochemical estimations. The dotted blue line indicates sea level. Redoubt summit peak is ~ 3 km ASL. Sample E5C1 – X1 depth is plotted in comparison. Orange symbols represent upper estimates. Blue symbols represent lower estimates. Squares are concentrations calculated using areas determined by Method 2. Circles are concentrations calculated using areas determined by Method 3. The uncertainty for the sample is ± 30 %.

5. Discussion

Calculated plagioclase H_2O concentrations varied from 12 ± 4 – 1165 ± 350 ppm (1σ). Calculated depths range from 0.12 ± 0.04 to > 34 km. The depth ranges generally do not agree with petrologic estimations of storage depths given by Coombs et al. (2013) (4 – 6 km) and Hosseini et al. (2023) (4.9 – 12.3 km), though Coombs et al. (2013) suggests a LSA deep source region situated between 30 – 40 km. Additionally, the depth ranges do not agree with geodetic estimations of mid-crustal storage of 10 – 14.5 km or deep magma injections occurring at > 23 km (Grapenthin et al., 2013). There is some agreement between calculated depths and geophysical observations of seismic activity. The shallowest sample, E5C1 – X1, falls within the range of hypocenter depths observed during the P1 seismic swarm (0 – 7 km; Bull and Buurman, 2013; Buurman et al., 2013). All studied crystals fall outside the range of mid-crustal seismicity (3 – 9 km; Power et al., 2013). However, there may be some agreement with the deep long period-earthquakes (DLPs) that occurred between 28 – 41 km in December of 2008 (Power et al., 2013).

Samples were prepared by two different methods (cut vs. single slab) and water concentrations were calculated by three different methods. Water concentrations were calculated using all three methods on sample E5C4 – X1. The difference in calculated lower and upper water concentration estimates between the three methods are

summarized in Table 4. Method 1 and Method 3 were closest in difference, suggesting that structural OH^- is dominantly expressed spectrally on one of three axes; the remaining two axes contribute similar spectral areas and are less than the first axis as opposed to all three axes have approximately equal spectral contributions, i.e., Method 3: $A_{tot} = A_x + 2A_y$ where $A_x > A_y \approx$ Method 1: $A_{tot} = A_x + A_y + A_z$ versus Method 2: $A_{tot} = (3/2)(A_x + A_y)$. This is similar to the spectral behavior observed by Castilla Montagut (2022) (e.g., see Figure 18 therein). However, this comparison was only done with one set of samples. More comparisons are required to see if this behavior is consistent. If this behavior is consistent, this would suggest that a simpler single slab preparation method is sufficient for studies using spot analyses that are not concerned with the presence of diffusional concentration gradients present on certain axes.

Table 4: Summarized difference in water concentration calculation between methods 1, 2, and 3.

Sample	Estimate Type	Method 1 vs. Method 2	Method 1 vs. Method 3	Method 2 vs. Method 3
E5C4 – X1 – H1	Upper Estimate (ppm)	6	0	6
	Lower Estimate (ppm)	1	2	3
E5C4 – X1 – H2	Upper Estimate (ppm)	14	0	14
	Lower Estimate (ppm)	9	2	9

The H_2O concentrations measured in the crystals fall towards the higher end, or in some cases overshoot, values reported in the literature. For example, many of the volcanic plagioclase water concentrations in Johnson & Rossman (2004) are in the 10s ppm, with some in the 100 – 300 ppm range, and one value going up to 510 ppm (see Table 1 in Johnson & Rossman (2004)). As pertains to this study's samples, there are three possible explanations for the high water concentrations measured:

1. The water concentrations measured are representative of concentrations present in the plagioclase phenocrysts, and these phenocrysts record a very deep crustal signature.
2. The partition coefficient (0.002) used to calculate wt % H_2O in the melt is incorrect.
3. There is spectral contribution within the measured spectral area that is not structurally bound OH^-.

Alaska's crust has been estimated to be as thick as 43 km (Zhang et al., 2019), meaning samples recording water contents near this depth are theoretically plausible. However, this

first explanation may be ruled out as the calculated wt % H_2O in the melt, confining pressure, and depth recorded by these phenocrysts indicate unrealistic values (e.g., up to 58 wt % H_2O in the melt, pressures >> 10,000 bars, and depths >> 40 km). The second explanation may be plausible; there are many uncertainties in feldspar-melt H partition coefficients (see Mosenfelder et al. (2015) and Hamada et al. (2013)). That said, the partition coefficient used in this study (0.002) has been used in other studies (Castilla Montagut, 2022; Rappoccio et al., 2020; Caseres, 2019; Mosenfelder et al., 2018) for dacitic to rhyolitic systems and has produced realistic depths. However, it is important to note that plagioclase-melt partition coefficients were determined for basaltic systems. It is debatable how valid the application of this study's chosen partition coefficient is given that Redoubt's system composition is primarily andesitic. The third explanation appears most likely and will be focused on for the remainder of the discussion.

There may be additional spectral contributions to the measured peak area that are not from OH^- that is structurally bound in plagioclase. Other peak contributors include C – H bonds from organics contamination, atmospheric H_2O, or melt inclusions, mineral inclusions, and fluid inclusions containing H. Atmospheric water may be ruled out as all samples were run under a purge-gas collar which removed atmospheric CO_2 and H_2O. The other possible contributing sources may be identified visually (melt, mineral, and fluid inclusions) and spectrally (melt and fluid inclusions, and organics contamination). Visually, inclusions appear as "bubbles" or "pockets" in the phenocryst. Melt inclusions generally appear brown but may be clear. Fluid inclusions are clear and may have visible vapor bubbles. To visually identify the presence of melt inclusions, mineral inclusions, and fluid inclusions, analyzed samples were put under a microscope and the spot area that was measured using FTIR was looked at under reflected and transmitted plane polarized light. In all crystals, the spots analyzed contained fluid inclusions. Some spots contained melt inclusions and/or mineral inclusions. Visual examples of inclusions are provided in Figure 13. Visual identifications are summarized in Table 5. See supplemental materials for a complete gallery of microscope pictures.

To spectrally identify melt and fluid inclusions, and organics contamination, spectra were examined to look for distinct peaks associated with each type of feature. Structurally bound OH^- in plagioclase has a peak centered around 3200 cm^{-1} with a "shoulder" typically occurring between 3600 cm^{-1} and 3550 cm^{-1}(Figure 14). Melt inclusions show up as an asymmetric peak skewed to the right and located between 3600 – 2700 cm^{-1}(Figure 15). Fluid inclusions show up a peak centered at around 3450 cm^{-1} with a spectral shoulder at 3270 cm^{-1} (Figure 15). Spectrally, organics contamination shows up as a cluster of three peaks between 3000 cm^{-1} and 2800 cm^{-1} (Figure 16). It is important to clarify that the focus of this analysis is not to identify whether an inclusion is a "melt" or a "fluid", but simply that it is present and may have contributed spectral signal to the OH^- peak.

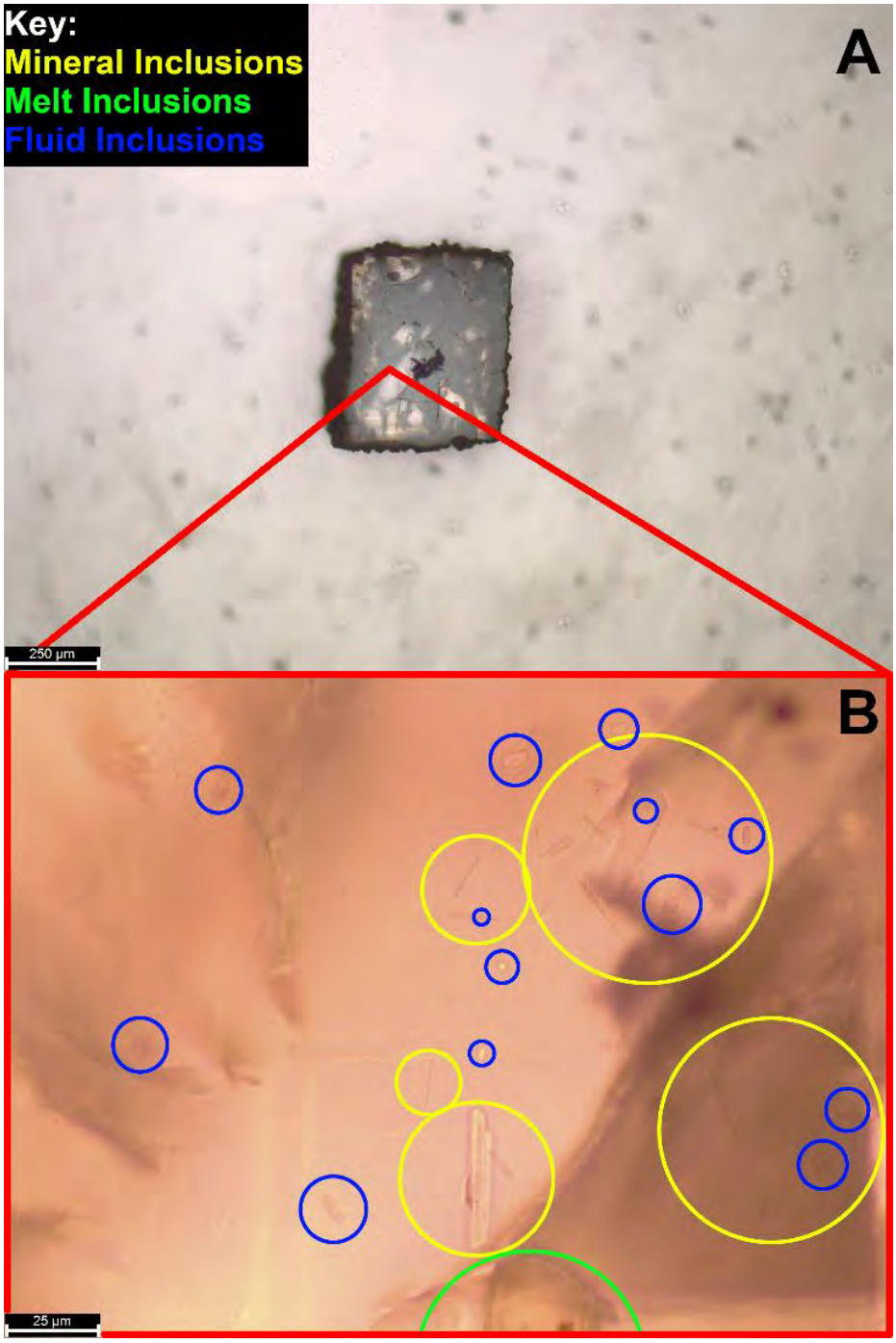

Figure 13: (A) Sample RED09-E5C4-X1-H1 under reflected light (x5 optic). (B) Area of analysis under transmitted light (x50 optic). Mineral, melt, and fluid inclusions are all present in this area and may have intersected the IR beam path during measurement. Yellow circles indicate mineral inclusions. Green circles indicate melt inclusions. Blue circles indicate fluid inclusions. See supplementary materials for a complete gallery of every sample.

Table 5: Visual identification of fluid inclusions, melt inclusions, and mineral inclusions at the spot measurement area. "O" indicates feature was present, "X" indicates feature was absent, "?" indicates it is unclear if the feature was present.

Sample	Fluid Inclusions	Melt Inclusions	Mineral Inclusions
E5C1 – X1	O	X	X
E5C2 – X1	O	?	X
E5C4 – X1 – H1	O	?	?
E5C4 – X1 – H2	O	X	X
E6C1 – X1	O	X	?
E6C1 – X2	O	?	X
E6C1 – X3	O	X	X
E6C1 – X4	O	?	?
E6C1 – X5	O	?	X
E6C1 – X6	O	?	?
E6C1 – X7	O	X	X
E6C2 – X1	O	X	X

Spectral identifications are summarized in Table 6. See supplemental materials for a complete gallery of spectral images.

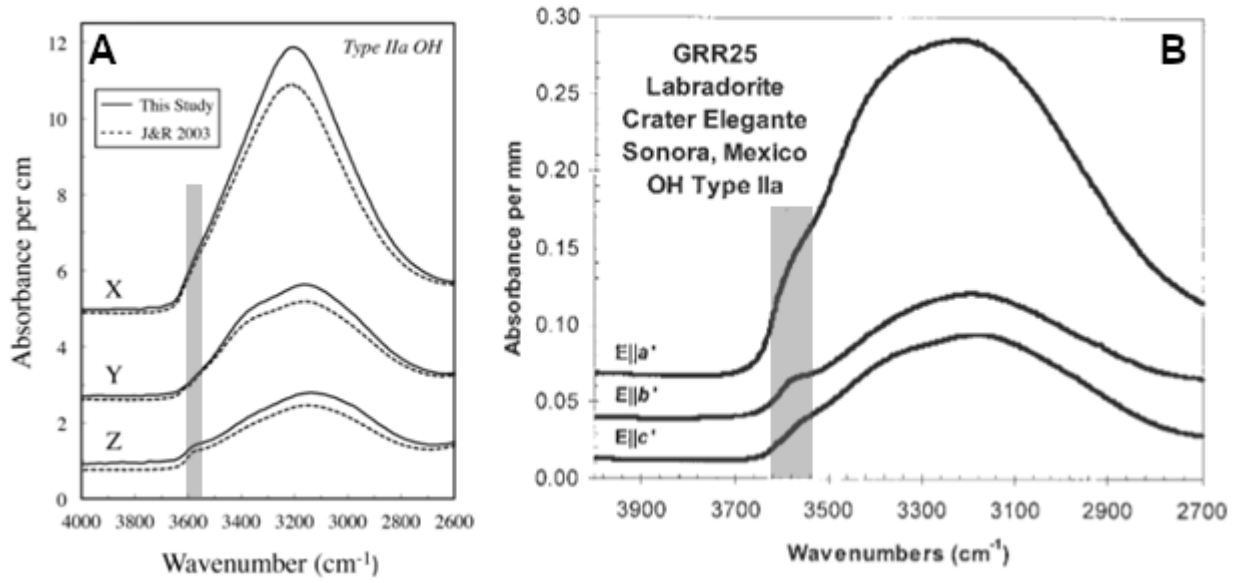

Figure 14: (A) OH^- spectral peaks of a Type IIa plagioclase feldspar from Figure 1a of Mosenfelder et al. (2015). (B) OH^- spectral peaks of a Type IIa plagioclase feldspar from Fig 1d of Johnson and Rossman (2004). The gray bar highlights the structural OH^- "shoulder" typically occurring between 3600 cm^{-1} and 3550 cm^{-1}.

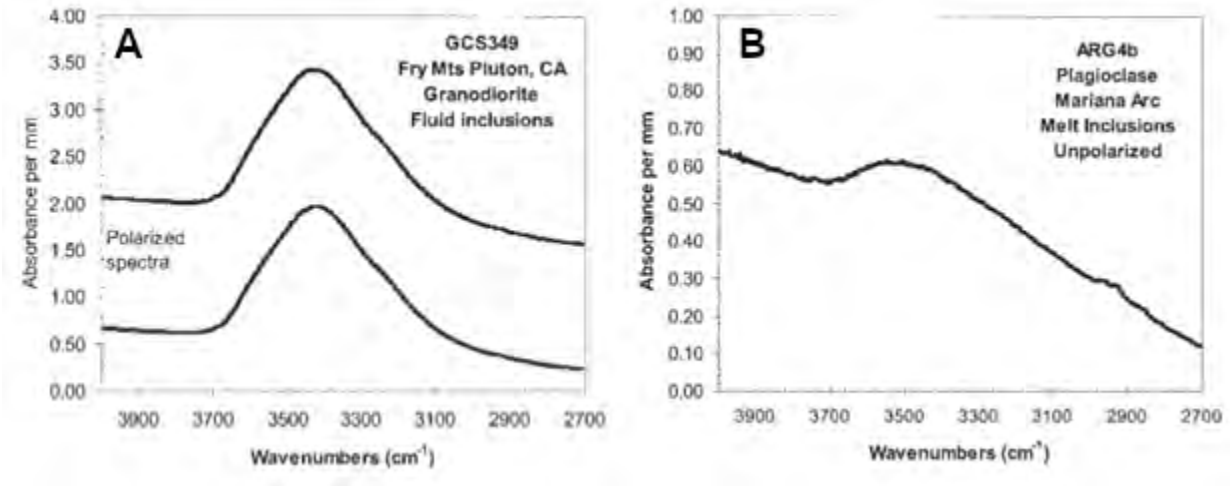

Figure 15: (A) Spectra of fluid inclusions in a volcanic plagioclase feldspar from Figure 1e of Johnson and Rossman (2004). Notice the peak at 3450 cm^{-1} with a spectral shoulder at 3270 cm^{-1}. (B) Unpolarized spectra of melt inclusions from Figure 1f of Johnson and Rossman (2004). Notice asymmetric peak skewed to the right.

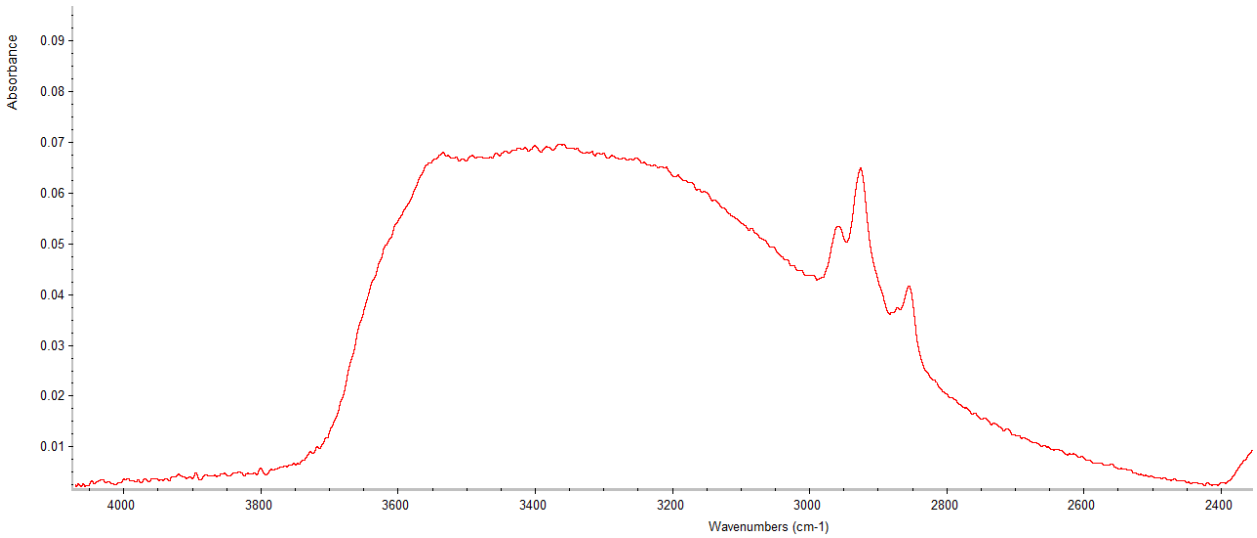

Figure 16: Example of spectral OH^- peak taken on sample RED09-E5C4-X1-H1-P00 with organics peaks present.

Table 6: Spectral identification of peaks associated with fluid inclusions, melt inclusions, and organics. "O" indicates feature was present, "X" indicates feature was absent, "?" indicates it is unclear if the feature was present.

Sample	Fluid Inclusions**		Melt Inclusions††		Organics‡‡	
E5C1 – X1	?	?	X	X	O	O
E5C2 – X1	?	?	?	X	O	X
E5C4 – X1 – H1	?	?	O	O	O	O
E5C4 – X1 – H2	?	?	X	O	O	O
E6C1 – X1	O	O	X	X	O	O
E6C1 – X2	O	O	X	X	X	X
E6C1 – X3	?	?	?	X	O	X
E6C1 – X4	?	O	X	X	X	X
E6C1 – X5	?	?	X	X	O	O
E6C1 – X6	?	X	?	X	O	X
E6C1 – X7	?	O	?	?	O	O
E6C2 – X1	?	?	X	X	O	O

Sample E5C1-X1 is particularly notable as it records a depth significantly shallower than the rest of the samples analyzed. Visual analysis shows that there are minimal fluid inclusions and no melt or mineral inclusions in the analysis area (see supplementary materials). Spectrally, no obvious fluid or melt inclusion signals are present, though there is organics contamination. This indicates that the true depth is shallower than was calculated. Sample E5C1-X1 may record an anomalously shallow depth (compared to other sample in our dataset) for a few reasons: the relative absence of cracks and inclusions suggests these features are a significant source of OH^- signal contribution to spectra, and in their absence, a more representative concentration of H_2O in plagioclase may be recorded. This sample likely re-equilibrated in the upper crust preceding eruption, overprinting past signals of deeper storage. This crystal may represent non-juvenile conduit or plug material entrained during eruption of Event 5 material or the stalling of Event 5 magma in the shallow crust preceding eruption.

The concentration of water in plagioclase relates to the storage depth and the over- and underestimation of water concentration because of study methodologies and assumptions indicate that these concentrations are not the true depths recorded by these crystals. Spectral contributions to the OH^- peak from sources that were not structurally bound OH^- likely overestimate the true storage depths of these crystals. Additionally, most spectra

** Fluid inclusions have a peak at 3450 cm^{-1} and a shoulder at 3270 cm^{-1} (Johnson and Rossman, 2004).
†† Melt inclusions have an asymmetric peak skewed to the right (Johnson and Rossman, 2004).
‡‡ C – H bonds spectrally have three peaks clustered between 3000^{-1} and 2800^{-1} (Johnson and Rossman, 2004).

only have two of three perpendicular axes measured, meaning the total water concentration may have been over or underestimated depending on the area calculation method used. However, the minimal difference in calculated water concentrations between sample preparation methods 1, 2 and 3 suggest that the simpler single doubly polished slab method is acceptable for applications only concerned with spot analyses (as opposed to traverse analyses, where diffusional gradients may be preserved along certain axes). When calculating the confining pressure, the VolatileCalc software did not have an input for the chemical system of Redoubt (andesitic), and so the closest option available was selected (basalt system, 49 wt % SiO_2). It is unclear what the behavior of a more silica rich system would be. The derived temperature (925 °C) averaged from FeTi measurements of Coombs et al. (2013) lies outside the ±200 °C acceptability range of the 1200 °C reference temperature, meaning the assumption regarding negligible temperature dependence on volatile solubility as is assumed by the basaltic system calculation (Newman & Lowenstern, 2002; Dixon et al., 1995) was violated. The CO_2 concentration was set to 0 ppm; however, it is more than likely that the system did have a CO_2 component (in addition to other volatiles). Coombs et al. (2013) suggests that based on the amount of CO_2 emitted over Redoubt Volcano's complete eruptive sequence (2.3 metric tons; Werner et al., 2013), it would constitute ~8000 ppm of the erupted magma. Werner et al., (2013) suggests 0.9 – 2.1 wt % CO_2. Plagioclase and pyroxene melt inclusions measured by Hosseini et al. (2023) indicate CO_2 concentration of <100 to ~1100 ppm, with plagioclase hosted melt inclusion bubbles having higher CO_2 than pyroxene hosted melt inclusion bubbles (1135 vs. 455 ppm CO_2). Using the volatile solubility model of Papale et al. (2006) to a dacitic liquid in LSA at certain petrologically inferred conditions, a ~2.7 wt % CO_2 vapor at shallow storage depths is predicted. Additionally, this calculation suggests a vapor composition of ~75 mol% H_2O and ~25 mol% CO_2 in the upper crustal storage region. Whether or not this condition is reflected at deeper depths is unknown but suggests a deeper storage depth for analyzed samples if the system did have CO_2 present.

6. Suggestions for Future Work

The following section provides some suggestions to guide future work but is by no means exhaustive. Topics range from the basis of partitioning and diffusion values for plagioclase feldspar, to uncertainties introduced during concentration calculations, general work to be done in the field of volcanology, and Redoubt-specific suggestions.

The plagioclase hygrometer is a relatively new technique with which water contents of host melts may be determined. As such, any work using this hygrometer would greatly contribute to the existing body of knowledge. In particular, expanding its use to volcanic systems of compositions that have yet to be analyzed is paramount to ascertaining our understanding of water diffusion in plagioclase as well as the plagioclase hygrometer's

potential applications in systems for which existing partitioning and diffusion characteristics have not yet been studied.

Our understanding of the partitioning and diffusive behavior of water in plagioclase is still in its infancy. Any future applications of the plagioclase hygrometer would be better supported by more experimental work to constrain partitioning and diffusion behavior. Among the many aspects which could be investigated, understanding if the plagioclase-melt partitioning behavior of water is Herian (i.e., constant or variable with pressure, temperature, composition, etc.) and if the diffusion of water in plagioclase is isotropic are essential. Furthermore, the dataset contributing to our understanding of the molar absorption coefficient is small and was significantly influenced by feldspars with compositions dissimilar to this study's samples (Mosenfelder et al., 2015). Studies investigating the change in the calibration curve with incorporation of more plagioclase composition feldspars are suggested.

As of this study, the choice of "appropriate" baseline correction is subjective and represents a large source of uncertainty (15 – 30 %) in the determination of integrated absorbance of a spectrum (Peslier & Luhr, 2006; Rossman, 2006; Koga et al., 2003). As it is subjective, no widely accepted and formalized method has been published. In some cases, automation of baseline corrections has been used where processing of large datasets quickly is required. Existing baseline correction methods have been developed for certain spectroscopic methods (e.g., FTIR, Raman, and NMR) and sample types (e.g., minerals, aerosols, etc.) (Giguere et al., 2015). However, automatic baseline correction methods are developed through ad hoc experimental tuning and there are no methods known to the author that are generally applicable and which may introduce consistent systematic error (Giguere et al., 2015). A formalized method for picking baselines under spectral OH^- curves is essential if the elimination of large uncertainties in association with human variability is to occur.

Current petrologic tools constraining hour to month timescales of pre-eruptive magma migration lack depth resolution which could be used in interpreting seismic signals through time and space. Water concentration gradients in plagioclase caused by diffusive loss during magmatic ascent provide an opportunity for geochemical chronology studies. Diffusive studies (Johnson and Rossman, 2013) have shown that water in plagioclase diffuses in days to weeks; importantly, these timescales are similar to seismic swarms occurring prior to the 2009 eruption of Redoubt (Schaefer, 2012). It has been suggested that this seismic swarm may have been related to magma migration at depth (Coombs et al., 2013). Future work using the plagioclase hygrometer on samples of the 2009 eruption of Redoubt should attempt to determine the presence of concentration gradients and a probable chronology of diffusive water loss as it relates to the pre-eruptive seismic record (i.e., is there any chronologic relationship between depths recorded by plagioclase and hypocenter depths of seismic swarms).

Lastly, to acquire the most accurate data, samples must be oriented along a principal crystallographic axis, free of impurities, optically clear, and polished to a perfectly smooth surface. Difficulties in finding and preparing ideal natural samples in this study impacted measurements; future studies working with 2009 Redoubt samples should ideally select "cleaner" grains as well as polish and clean samples better than was achieved in this study. Alternatively, future studies could reduce the influence of spectrally contributing inclusions by polishing thinner slabs, using FTIR array detectors to locate areas of lower water concentration (and by proxy, less inclusions), or measuring water through Secondary Ion Mass Spectrometry (SIMS) which samples at a relatively shallow level that is ideally inclusion-free, meaning a more representative water concentration value can be measured. Additionally, more analyzed samples would contribute to the limited amount of plagioclase hygrometer-derived depth values. Future studies should also investigate the differences in calculated water concentration between cut slabs and single slabs using different area calculation equations. This would not only inform future methods for more reliable sample preparation (i.e., single slabs versus cut slabs) but would also provide insight into the nature of the structural distribution of OH^- in plagioclase feldspar.

7. Conclusions and Broader Implications

Water in plagioclase feldspar crystals from Event 5 and Event 6 of the 2009 eruption of Redoubt Volcano was measured. Calculated plagioclase H_2O concentrations varied from 8.8 ± 2.6 – 1165 ± 350 ppm (1σ). Calculated depths ranged from 0.12 ± 0.04 to > 34 km (1σ). The depth ranges generally do not agree with petrologic or geodetic estimations of magma storage depths, apart from a posited deep storage region between 30 – 40 km depth. However, there is some agreement with the geophysical record, including overlap with the range of hypocenter depths observed during the P1 seismic swarm (0 – 7 km) as well as with DLPs (28 – 41 km), around the deep, diffuse magma source region.

Issues associated with study samples, methodology, and assumptions complicate interpretation. Of the eleven samples analyzed, only one sample (E5C1 – X1) was determined to represent a relatively clean structural OH^- signal. The recorded depth of this sample ranged from 0.12 ± 0.04 km to 0.28 ± (0.08) km. Explanations for this shallow depth include re-equilibration in the upper crust preceding eruption (overprinting of past signals of deeper storage) or that this crystal may represent non-juvenile material present in a plug or conduit that was entrained during eruption of Event 5 material or the stalling of Event 5 magma in the shallow crust preceding eruption.

The plagioclase hygrometer, if applied appropriately, could be a broadly applicable and reliable indicator of host melt water contents. Sample selection and preparation, study methodology, and assumed constants factoring into a depth calculation must be carefully considered to evaluate the validity of study findings using this method. This study may

contribute not only to our understanding of the Redoubt Volcanic system, but to volcanic systems on a global scale. Much future work is required to address all aspects of the plagioclase hygrometry technique. If proven reliable, the plagioclase hygrometer may greatly contribute to our ongoing effort to mechanistically understand the processes driving volcanic eruptions and may have the potential to help save the lives of people around the world for many years to come.

Acknowledgements

Thank you to the Alaska Volcano Observatory for providing the Event 5 and Event 6 pyroclast samples used in this study. Thank you to the University of Maryland, Department of Geology for its Senior Thesis program; you provide undergraduate students with an opportunity to create something new, something exciting, something that they may call their own. This program holds no equal.

To my faculty advisor Dr. Megan E. Newcombe: thank you for your guidance, kindness, patience, and professionalism. Even when faced with my failings as a student and a person, you stood by me and helped me see this project through. I hold great respect for you and hope you will take me in kind.

To my graduate student advisor Sumedha Desikamani: it has been my pleasure to get to know you over these last nine months. I could not have asked for a kinder, more intelligent, and dedicated advisor. Thank you for the many hours of back-and-forth, reviewing my seemingly endless flow of drafts, and being a good sport whenever I roped you into my antics. I truly could not have made this thesis what it is without you. For whatever this thesis is worth, I consider its success yours as much as it is mine. It is my privilege to call you a friend.

To the director of the Senior Thesis program, Dr. Philip M. Piccoli: you are a mentor, and you are my friend. This program would not be what it is today without your dedication to the students and this department. Thank you for allowing me to barge into your office at all hours of the day, humoring my half-baked ideas, nurturing my own interests, and guiding me through the research process. Of course, thank you for all the free fruit. It was tasty.

Thank you to all members of the UMD Planetary Volcanism Laboratory. To Kathy Stepien: here is to all the great many hours we spent together in the lab grumbling over polishing, Nicolet, and the generalized malady which we may label “education”. Things are never boring when you are around. Thank you for your friendship. To Dr. Liam Peterson: thank you for all your input on this project. I hope to be as jaded, cynical, and curmudgeonly as you one day. I guess that is something that comes with a doctorate. To Cosmo Varah-Sikes: here is your shout-out. I believe you owe me two dollars now. Your antics inspired my daily amicable harassment of my group mates. To Kyle Kim: thank you for always supporting my predilection to desiccant consumption. You and you alone afforded me this kindness.

From the bottom of my heart, thank you to C.H. and H.N. for being true friends in trying times. I could not have completed this thesis without your support. Here is to many more years of friendship.

I dedicate this work in memory of J.L. and A.L. Thank you for having let me be a part of your lives. You are as much a part of me now as you were then.

Supplementary Material

Supplementary material consisting of clast and inclusion pictures, concentration and depth calculations, figures, FTIR spot analysis data, and a copy of the VolatileCalc program has been provided in the following compressed file:

Robert_Stutzke_GEOL394_SuppMat.rar

This file can be accessed on the University of Maryland Geology Department's online file repository.

Bibliography

Bacon, C.R., Vazquez, J.A., Wooden, J.L., 2012. Peninsular terrane basement ages recorded by Paleozoic and Paleoproterozoic zircon in gabbro xenoliths and andesite from Redoubt volcano, Alaska. Bulletin of the Geological Society of America 124, 24–34. https://doi.org/10.1130/B30439.1

Begét, J.E., Nye, C.J., 1994. Postglacial eruption history of Redoubt Volcano, Alaska. Journal of Volcanology and Geothermal Research 62, 31–54.

Behrens, H., 2021. Hydrogen defects in feldspars: defect properties and implications for water solubility in feldspar. Phys Chem Miner 48, Article Number 27. https://doi.org/10.1007/s00269-020-01128-0

Bell, D.R., Rossman, G.R., 1992. Water in Earth's Mantle: The Role of Nominally Anhydrous Minerals Articles Water in Earth's Mantle: The Role of Nominally Anhydrous Minerals. Science (1979) 255, 1391–1397.

Blank, J.G., Stolper, E.M., Carroll, M.R., 1993. Solubilities of carbon dioxide and water in rhyolitic melt at 850°C and 750 bars. Earth Planet Sci Lett 119, 27–36.

Bleick, H.A., Coombs, M.L., Cervelli, P.F., Bull, K.F., Wessels, R.L., 2013. Volcano-ice interactions precursory to the 2009 eruption of Redoubt Volcano, Alaska. Journal of Volcanology and Geothermal Research 259, 373–388. https://doi.org/10.1016/j.jvolgeores.2012.10.008

Brantley, S.R., 1990. The Eruption of Redoubt Volcano. Alaska, December 14, 1989-August 31. U.S. Geological Survey Circular 1061, 1–33.

Bucholz, C.E., Gaetani, G.A., Behn, M.D., Shimizu, N., 2013. Post-entrapment modification of volatiles and oxygen fugacity in olivine-hosted melt inclusions. Earth Planet Sci Lett 374, 145–155. https://doi.org/10.1016/j.epsl.2013.05.033

Bull, K.F., Buurman, H., 2013. An overview of the 2009 eruption of Redoubt Volcano, Alaska. Journal of Volcanology and Geothermal Research 259, 2–15. https://doi.org/10.1016/j.jvolgeores.2012.06.024

Buurman, H., West, M.E., Thompson, G., 2013. The seismicity of the 2009 Redoubt eruption. Journal of Volcanology and Geothermal Research 259, 16–30. https://doi.org/10.1016/j.jvolgeores.2012.04.024

Caseres, J.R., 2019. Water and Fluorine Contents in Mt. Hood Magmas Recorded by Plagioclase Phenocrysts. University of Minnesota, Master's Thesis.

Caseres, J.R., Mosenfelder, J.L., Hirschmann, M.M., 2018. H_2O and F contents in Mt. Hood magmas recorded by plagioclase phenocrysts, in: AGU Fall Meeting Abstracts. American Geophysical Union, Fall Meeting 2018, abstract #V43I-0249.

Castilla Montagut, S.C., 2022. Rapid Destabilization of Deep, Superhydrous Magma Prior to the Largest Known Eruption of Cerro Machin Volcano, Colombia. University of Maryland, Master's Thesis.

Christensen, N.I., Mooney, W.D., 1995. Seismic velocity structure and composition of the continental crust: a global view. J Geophys Res 100, 9761–9788. https://doi.org/10.1029/95JB00259

Cioni, R., Pistolesi, M., Bertagnini, A., Bonadonna, C., Hoskuldsson, A., Scateni, B., 2014. Insights into the dynamics and evolution of the 2010 Eyjafjallajökull summit eruption (Iceland) provided by volcanic ash textures. Earth Planet Sci Lett 394, 111–123. https://doi.org/10.1016/j.epsl.2014.02.051

Coombs, M.L., Sisson, T.W., Bleick, H.A., Henton, S.M., Nye, C.J., Payne, A.L., Cameron, C.E., Larsen, J.F., Wallace, K.L., Bull, K.F., 2013. Andesites of the 2009 eruption of Redoubt Volcano, Alaska. Journal of Volcanology and Geothermal Research 259, 349–372. https://doi.org/10.1016/j.jvolgeores.2012.01.002

Crank, J., 1975. The mathematics of diffusion, Second. ed. Oxford University Press.

Demouchy, S., Jacobsen, S.D., Gaillard, F., Stem, C.R., 2006. Rapid magma ascent recorded by water diffusion profiles in mantle olivine. Geology 34, 429–432. https://doi.org/10.1130/G22386.1

Detterman, R.L., Case, J.E., WIlson, F.H., 1980. Paleozoic rocks on the Alaska Peninsula, in: Detterman, R.L., Case, J.E. (Eds.), United States Geological Survey in Alaska: Accomplishments during 1978. U.S. Geological Survey , pp. B85–B86.

Dixon, J.E., 1997. Degassing of alkalic basalts. American Mineralogist 82, 368–378.

Dixon, J.E., Stolper, E.M., Holloway, J.R., 1995. An Experimental Study of Water and Carbon Dioxide Solubilities in Mid-Ocean Ridge Basaltic Liquids. Part I: Calibration and Solubility Models. Journal of Petrology 36, 1607–1631.

Dixon, J.P., Stihler, S.D., Power, J.A., Searcy, C.K., 2010. Catalog of earthquake hypocenters at Alaskan volcanoes: January 1 through December 31, 2009: U.S. Geological Survey Data Series 531.

Dorava, J.M., Meyer, D.F., 1994. Hydrologic hazards in the lower Drift River basin associated with the 1989-1990 eruptions of Redoubt Volcano, Alaska. Journal of Volcanology and Geothermal Research 62, 387–407.

Ekstrand, A.L., Webley, P.W., Garay, M.J., Dehn, J., Prakash, A., Nelson, D.L., Dean, K.G., Steensen, T., 2013. A multi-sensor plume height analysis of the 2009 Redoubt eruption. Journal of Volcanology and Geothermal Research 259, 170–184. https://doi.org/10.1016/j.jvolgeores.2012.09.008

Fee, D., McNutt, S.R., Lopez, T.M., Arnoult, K.M., Szuberla, C.A.L., Olson, J. V., 2013. Combining local and remote infrasound recordings from the 2009 Redoubt Volcano eruption. Journal of Volcanology and Geothermal Research 259, 100–114. https://doi.org/10.1016/j.jvolgeores.2011.09.012

Gardner, C.A., Neal, C.A., Waitt, R.B., Janda, R.J., 1994. Proximal pyroclastic deposits from the 1989-1990 eruption of Redoubt Volcano, Alaska Stratigraphy, distribution, and physical characteristics. Journal of Volcanology and Geothermal Research 62, 213–250.

Giguere, S., Carey, C.J., Boucher, T., Mahadevan, S., Darby Dyar, M., 2015. An Optimization Perspective on Baseline Removal for Spectroscopy. Physics (College Park Md).

Grapenthin, R., Freymueller, J.T., Kaufman, A.M., 2013. Geodetic observations during the 2009 eruption of Redoubt Volcano, Alaska. Journal of Volcanology and Geothermal Research 259, 115–132. https://doi.org/10.1016/j.jvolgeores.2012.04.021

Hamada, M., Kawamoto, T., Takahashi, E., Fujii, T., 2011. Polybaric degassing of island arc low-K tholeiitic basalt magma recorded by OH concentrations in Ca-rich plagioclase. Earth Planet Sci Lett 308, 259–266. https://doi.org/10.1016/j.epsl.2011.06.005

Hamada, M., Ushioda, M., Fujii, T., Takahashi, E., 2013. Hydrogen concentration in plagioclase as a hygrometer of arc basaltic melts: Approaches from melt inclusion analyses and hydrous melting experiments. Earth Planet Sci Lett 365, 253–262. https://doi.org/10.1016/j.epsl.2013.01.026

Hosseini, B., Myers, M., Loewen, M., Wieser, P.E., DeVitre, C.L., Wallace, K.L., Coombs, M.L., 2023. Redoubt 2009 Revisited: A Melt Inclusion Perspective on the Source Region of the Low-Silica Andesite, in: AGU Fall Meeting Abstracts. American Geophysical Union, Fall Meeting 2023.

Hotovec, A.J., Prejean, S.G., Vidale, J.E., Gomberg, J., 2013. Strongly gliding harmonic tremor during the 2009 eruption of Redoubt Volcano. Journal of Volcanology and Geothermal Research 259, 89–99. https://doi.org/10.1016/j.jvolgeores.2012.01.001

Jakobsson, S., 1997. Solubility of water and carbon dioxide in an icelandite at 1400°C and 10 kilobar. Contributions to Mineralogy and Petrology 127, 129–135.

Jirasek, A., Schulze, G., Yu, M.M.L., Blades, M.W., Turner, R.F.B., 2004. Accuracy and Precision of Manual Baseline Determination. Appl Spectrosc 58, 1488–1499.

Johnson, E.A., Rossman, G.R., 2013. The diffusion behavior of hydrogen in plagioclase feldspar at 800-1000 °C: Implications for re-equilibration of hydroxyl in volcanic phenocrysts. American Mineralogist 98, 1779–1787. https://doi.org/10.2138/am.2013.4521

Johnson, E.A., Rossman, G.R., 2004. A survey of hydrous species and concentrations in igneous feldspars. American Mineralogist 89, 586–600.

Johnson, E.A., Rossman, G.R., 2003. The concentration and speciation of hydrogen in feldspars using FTIR and 1H MAS NMR spectroscopy. American Mineralogist 88, 901–911.

Kahl, M., Chakraborty, S., Costa, F., Pompilio, M., 2011. Dynamic plumbing system beneath volcanoes revealed by kinetic modeling, and the connection to monitoring data: An example from Mt. Etna. Earth Planet Sci Lett 308, 11–22. https://doi.org/10.1016/j.epsl.2011.05.008

Ketner, D., Power, J., 2013. Characterization of seismic events during the 2009 eruption of Redoubt Volcano, Alaska. Journal of Volcanology and Geothermal Research 259, 45–62. https://doi.org/10.1016/j.jvolgeores.2012.10.007

Kienle, J., Swanson, S.E., 1983. Volcanism in the eastern Aleutian arc: Late quaternary and holocene centers, tectonic setting and petrology. J. Volcanol. Geotherm. Res 17, 393–432.

Koga, K., Hauri, E., Hirschmann, M., Bell, D., 2003. Hydrogen concentration analyses using SIMS and FTIR: Comparison and calibration for nominally anhydrous minerals. Geochemistry, Geophysics, Geosystems 4. https://doi.org/10.1029/2002GC000378

Leonard, G.S., Stewart, C., Wilson, T.M., Procter, J.N., Scott, B.J., Keys, H.J., Jolly, G.E., Wardman, J.B., Cronin, S.J., McBride, S.K., 2014. Integrating multidisciplinary science, modelling and impact data into evolving, syn-event volcanic hazard mapping and communication: A case study from the 2012 Tongariro eruption crisis, New Zealand. Journal of Volcanology and Geothermal Research 286, 208–232. https://doi.org/10.1016/j.jvolgeores.2014.08.018

Libowitzky, E., Beran, A., 2006. The Structure of Hydrous Species in Nominally Anhydrous Minerals: Information from Polarized IR Spectroscopy, in: Keppler, H., Smyth, J.R. (Eds.), Water in Nominally Anhydrous Minerals. The Mineralogical Society of America, pp. 29–30.

Lindsay, J., Marzocchi, W., Jolly, G., Constantinescu, R., Selva, J., Sandri, L., 2010. Towards real-time eruption forecasting in the Auckland Volcanic Field: Application of BET_EF during the New Zealand National Disaster Exercise "Ruaumoko." Bull Volcanol 72, 185–204. https://doi.org/10.1007/s00445-009-0311-9

Lopez, T., Carn, S., Werner, C., Fee, D., Kelly, P., Doukas, M., Pfeffer, M., Webley, P., Cahill, C., Schneider, D., 2013. Evaluation of Redoubt Volcano's sulfur dioxide emissions by the Ozone Monitoring Instrument. Journal of Volcanology and Geothermal Research 259, 290–307. https://doi.org/10.1016/j.jvolgeores.2012.03.002

Martin, G.C., Katz, F.J., 1912. A Geologic Reconnaissance of the Iliamna Region, Alaska. US Government Printing Office.

Marzocchi, W., Bebbington, M.S., 2012. Probabilistic eruption forecasting at short and long time scales. Bull Volcanol 74, 1777–1805. https://doi.org/10.1007/s00445-012-0633-x

McNutt, S.R., Thompson, G., West, M.E., Fee, D., Stihler, S., Clark, E., 2013. Local seismic and infrasound observations of the 2009 explosive eruptions of Redoubt Volcano, Alaska. Journal of Volcanology and Geothermal Research 259, 63–76. https://doi.org/10.1016/j.jvolgeores.2013.03.016

Miller, T.P., Chouet, B.A., 1994. The 1989-1990 eruptions of Redoubt Volcano: An introduction. Journal of Volcanology and Geothermal Research 62, 1–1.

Moore, G., Vennemann, T., Carmichael, I.S.E., 1998. An empirical model for the solubility of H_2O in magmas to 3 kilobars. American Mineralogist 83, 36–42. https://doi.org/10.2138/am-1998-1-203

Mosenfelder, J.L., Andrys, J.L., von der Handt, A., Kohlstedt, D.L., Hirschmann, M.M., 2020. Hydrogen incorporation in plagioclase. Geochim Cosmochim Acta 277, 87–110. https://doi.org/10.1016/j.gca.2020.03.013

Mosenfelder, J.L., Caseres, J.R., Andrys, J., Wright, H.M.N., Hirschmann, M.M., 2018. Trace H and F Concentrations in Feldspar as Monitors of Volatile Processes in the Earth and Moon, in: AGU Fall Meeting Abstracts. American Geophysical Union, Fall Meeting 2018, abstract #MR23B-0085.

Mosenfelder, J.L., Rossman, G.R., Johnson, E.A., 2015. Hydrous species in feldspars: A reassessment based on FTIR and SIMS. American Mineralogist 100, 1209–1221. https://doi.org/10.2138/am-2015-5034

Mysen, B.O., Eggler, D.H., Seitz, M.G., Holloway, J.R., 1976. Carbon dioxide in silicate melts and crystals. Part I, Solubility measurements. Am J Sci 276, 455–479.

Newcombe, M.E., Plank, T., Zhang, Y., Holycross, M., Barth, A., Lloyd, A.S., Ferguson, D., Houghton, B.F., Hauri, E., 2020. Magma Pressure-Temperature-Time Paths During Mafic Explosive Eruptions. Front Earth Sci (Lausanne) 8. https://doi.org/10.3389/feart.2020.531911

Newman, S., Lowenstern, J.B., 2002. VolatileCalc: a silicate melt-H_2O-CO_2 solution model written in Visual Basic for Excel. Comput Geosci 28, 597–604.

Ogiso, M., Matsubayashi, H., Yamamoto, T., 2015. Descent of tremor source locations before the 2014 phreatic eruption of Ontake volcano, Japan 5. Volcanology. Earth, Planets and Space 67. https://doi.org/10.1186/s40623-015-0376-y

Papale, P., Moretti, R., Barbato, D., 2006. The compositional dependence of the saturation surface of H2O + CO2 fluids in silicate melts. Chem Geol 229, 78–95. https://doi.org/10.1016/j.chemgeo.2006.01.013

Peslier, A.H., Bizimis, M., Matney, M., 2015. Water disequilibrium in olivines from Hawaiian peridotites: Recent metasomatism, H diffusion and magma ascent rates. Geochim Cosmochim Acta 154, 98–117. https://doi.org/10.1016/j.gca.2015.01.030

Peslier, A.H., Luhr, J.F., 2006a. Hydrogen loss from olivines in mantle xenoliths from Simcoe (USA) and Mexico: Mafic alkalic magma ascent rates and water budget of the sub-continental lithosphere. Earth Planet Sci Lett 242, 302–319. https://doi.org/10.1016/j.epsl.2005.12.019

Peslier, A.H., Luhr, J.F., 2006b. Hydrogen loss from olivines in mantle xenoliths from Simcoe (USA) and Mexico: Mafic alkalic magma ascent rates and water budget of the sub-continental lithosphere. Earth Planet Sci Lett 242, 302–319. https://doi.org/10.1016/j.epsl.2005.12.019

Plank, T., Kelley, K.A., Zimmer, M.M., Hauri, E.H., Wallace, P.J., 2013. Why do mafic arc magmas contain ~4wt% water on average? Earth Planet Sci Lett 364, 168–179. https://doi.org/10.1016/j.epsl.2012.11.044

Poland, M.P., Anderson, K.R., 2020. Partly Cloudy with a chance of lava flows: Forecasting volcanic eruptions in the twenty-first century. J Geophys Res Solid Earth 125.

Power, J.A., Lahr, J.C., Page, R.A., Chouet, B.A., Stephens, C.D., Harlow, D.H., Murray, T.L., Davies, J.N., 1994. Seismic evolution of the 1989 - 1990 eruption sequence of Redoubt Volcano, Alaska. Journal of Volcanology and Geothermal Research 62, 69–94.

Power, J.A., Stihler, S.D., Chouet, B.A., Haney, M.M., Ketner, D.M., 2013. Seismic observations of Redoubt Volcano, Alaska - 1989-2010 and a conceptual model of the Redoubt magmatic system. Journal of Volcanology and Geothermal Research 259, 31–44. https://doi.org/10.1016/j.jvolgeores.2012.09.014

Rappoccio, R., Johnson, E.A., Myers, M., Wallace, P.J., Wilson, C.J.N., 2020. Hydroxyl in Quartz and Feldspar Phenocrysts from the Bishop Tuff, CA, and the Huckleberry Ridge Tuff, Yellowstone , in: AGU Fall Meeting Abstracts. pp. V003-0005.

Rasmussen, D.J., Plank, T.A., Roman, D.C., Power, J.A., Bodnar, R.J., Hauri, E.H., 2018. When does eruption run-up begin? Multidisciplinary insight from the 1999 eruption of Shishaldin volcano. Earth Planet Sci Lett 486, 1–14. https://doi.org/10.1016/j.epsl.2018.01.001

Rasmussen, D.J., Plank, T.A., Roman, D.C., Zimmer, M.M., 2022. Magmatic water content controls the pre-eruptive depth of arc magmas. Science (1979) 375, 1169–1172.

Reed, B.L., Lanphere, M.A., 1974. Chemical Variations Across the Alaska-Aleutian Range Batholith. Journal Research U.S. Geological Survey 2, 343–352.

Riehle, J.R., Kienle, J., Emmel, K.S., Hammond, J.S., Leresche, R.E., Haynes, G., 1981. Lahars in Crescent River Valley, Lower Cook Inlet, Alaska. Division of Geological & Geophysical Surveys.

Rose-Koga, E.F., Bouvier, A.S., Gaetani, G.A., Wallace, P.J., Allison, C.M., Andrys, J.A., Angeles de la Torre, C.A., Barth, A., Bodnar, R.J., Bracco Gartner, A.J.J., Butters, D., Castillejo, A., Chilson-Parks, B., Choudhary, B.R., Cluzel, N., Cole, M., Cottrell, E., Daly, A., Danyushevsky, L. V., DeVitre, C.L., Drignon, M.J., France, L., Gaborieau, M., Garcia, M.O., Gatti, E., Genske, F.S., Hartley, M.E., Hughes, E.C., Iveson, A.A., Johnson, E.R., Jones, M., Kagoshima, T., Katzir, Y., Kawaguchi, M., Kawamoto, T., Kelley, K.A., Koornneef, J.M., Kurz, M.D., Laubier, M., Layne, G.D., Lerner, A., Lin, K.Y., Liu, P.P., Lorenzo-Merino, A., Luciani, N., Magalhães, N., Marschall, H.R., Michael, P.J., Monteleone, B.D., Moore, L.R., Moussallam, Y., Muth, M., Myers, M.L., Narváez, D.F., Navon, O., Newcombe, M.E., Nichols, A.R.L., Nielsen, R.L., Pamukcu, A., Plank, T., Rasmussen, D.J., Roberge, J., Schiavi, F., Schwartz, D., Shimizu, K., Shimizu, N., Thomas, J.B., Thompson, G.T., Tucker, J.M., Ustunisik, G., Waelkens, C., Zhang, Y., Zhou, T., 2021. Silicate melt inclusions in the new millennium: A review of recommended practices for preparation, analysis, and data presentation. Chem Geol 570. https://doi.org/10.1016/j.chemgeo.2021.120145

Rossman, G.R., 2006. Analytical Methods for Measuring Water in Nominally Anhydrous Minerals. Rev Mineral Geochem 62, 1–28. https://doi.org/10.2138/rmg.2006.62.1

Ruth, D.C.S., Costa, F., Bouvet De Maisonneuve, C., Franco, L., Cortés, J.A., Calder, E.S., 2018. Crystal and melt inclusion timescales reveal the evolution of magma migration before eruption. Nat Commun 9. https://doi.org/10.1038/s41467-018-05086-8

Saunders, K., Blundy, J., Dohmen, R., Cashman, K., 2012. Linking petrology and seismology at an active volcano. Science (1979) 336, 1023–1027. https://doi.org/DOI: 10.1126/science.1220066

Schaefer, J.R., 2012. The 2009 Eruption of Redoubt Volcano, Alaska.

Schneider, D.J., Hoblitt, R.P., 2013. Doppler weather radar observations of the 2009 eruption of Redoubt Volcano, Alaska. Journal of Volcanology and Geothermal Research 259, 133–144. https://doi.org/10.1016/j.jvolgeores.2012.11.004

Scott, W.E., McGimsey, R.G., 1994. Character, mass, distribution, and origin of tephra-fall deposits of the 1989-1990 eruption of Redoubt Volcano, south-central Alaska. Journal of Volcanology and Geothermal Research 62, 251–272.

Seaman, S.J., Dyar, M.D., Marinkovic, N., Dunbar, N.W., 2006. An FTIR study of hydrogen in anorthoclase and associated melt inclusions. American Mineralogist 91, 12–20. https://doi.org/10.2138/am.2006.1765

Solana, M.C., Kilburn, C.R.J., Rolandi, G., 2008. Communicating eruption and hazard forecasts on Vesuvius, Southern Italy. Journal of Volcanology and Geothermal Research 172, 308–314. https://doi.org/10.1016/j.jvolgeores.2007.12.027

Soloman, G.C., Rossman, G.R., 1988. NH4+ in pegmatitic feldspars from the southern Black Hills, South Dakota. American Mineralogist 73, 818–821.

Sparks, R.S.J., Aspinall, W.P., 2004. Volcanic activity: Frontiers and challenges in forecasting, prediction and risk assessment, in: Geophysical Monograph Series. Blackwell Publishing Ltd, pp. 359–373. https://doi.org/10.1029/150GM28

Sturm, M., Benson, C., MacKeith, P., 1986. Effects of the 1966–68 Eruptions of Mount Redoubt on the Flow of Drift Glacier, Alaska, U.S.A. Journal of Glaciology 32, 355–362. https://doi.org/10.3189/s002214300001203x

Till, A.B., Yount, M.E., Bevier, M.L., 1994. The geologic history of Redoubt Volcano, Alaska. Journal of Volcanology and Geothermal Research 62, 11–30.

Trabant, D.C., Waitt, R.B., Major, J.J., 1994. Disruption of Drift glacier and origin of floods during the 1989-1990 eruptions of Redoubt Volcano, Alaska. Journal of Volcanology and Geothermal Research 62, 369–385.

Urann, B.M., Le Roux, V., Jagoutz, O., Müntener, O., Behn, M.D., Chin, E.J., 2022. High water content of arc magmas recorded in cumulates from subduction zone lower crust. Nat Geosci 15, 501–508. https://doi.org/10.1038/s41561-022-00947-w

Vancouver, G., 1984. A voyage of discovery to the North Pacific Ocean and round the world, 1791-1795 : with an introduction and appendices. Hakluyt Society.

Voyer, M. Le, Asimow, P.D., Mosenfelder, J.L., Guan, Y., Wallace, P., Schiano, P., Stolper, E.M., Eiler, J.M., 2014. Zonation of H_2O and F concentrations around melt inclusions in olivines. Journal of Petrology 55, 685–707. https://doi.org/10.1093/petrology/egu003

Wadge, G., Aspinall, W.P., 2014. Chapter 24 A review of volcanic hazard and risk-assessment praxis at the Soufrière Hills Volcano, Montserrat from 1997 to 2011. Geological Society of London, Memoirs 39, 439–456. https://doi.org/10.1144/m39.24

Wallace, K.L., Schaefer, J.R., Coombs, M.L., 2013. Character, mass, distribution, and origin of tephra-fall deposits from the 2009 eruption of Redoubt Volcano, Alaska-Highlighting the

significance of particle aggregation. Journal of Volcanology and Geothermal Research 259, 145–169. https://doi.org/10.1016/j.jvolgeores.2012.09.015

Wallace, P.J., 2005. Volatiles in subduction zone magmas: Concentrations and fluxes based on melt inclusion and volcanic gas data. Journal of Volcanology and Geothermal Research 140, 217–240. https://doi.org/10.1016/j.jvolgeores.2004.07.023

Wallace, P.J., Plank, T., Bodnar, R.J., Gaetani, G.A., Shea, T., 2021. Olivine-Hosted Melt Inclusions: A Microscopic Perspective on a Complex Magmatic World. Annu Rev Earth Planet Sci 49, 465–494. https://doi.org/10.1146/annurev-earth-082420

Waythomas, C.F., Pierson, T.C., Major, J.J., Scott, W.E., 2013. Voluminous ice-rich and water-rich lahars generated during the 2009 eruption of Redoubt Volcano, Alaska. Journal of Volcanology and Geothermal Research 259, 389–413. https://doi.org/10.1016/j.jvolgeores.2012.05.012

Werner, C., Kelly, P.J., Doukas, M., Lopez, T., Pfeffer, M., McGimsey, R., Neal, C., 2013. Degassing of CO2, SO2, and H2S associated with the 2009 eruption of Redoubt Volcano, Alaska. Journal of Volcanology and Geothermal Research 259, 270–284. https://doi.org/10.1016/j.jvolgeores.2012.04.012

Yang, X., 2012. An experimental study of H solubility in feldspars: Effect of composition, oxygen fugacity, temperature and pressure and implications for crustal processes. Geochim Cosmochim Acta 97, 46–57. https://doi.org/10.1016/j.gca.2012.08.036

Zhang, Y., Li, A., Hu, H., 2019. Crustal Structure in Alaska From Receiver Function Analysis. Geophys Res Lett 46, 1284–1292. https://doi.org/10.1029/2018GL081011

University of Maryland Honor Statement

I pledge on my honor that I have not given or received any unauthorized assistance on this assignment/examination.

Robert Allen Stutzke